2016

Numerical Solution of the Electron Heat Transport Equation and Physics-Constrained Modeling of the Thermal Conductivity via Sequential Quadratic Programming Optimization in Nuclear Fusion Plasmas

Zachary John Pelli
Lehigh University

Numerical Solution of the Electron Heat Transport Equation and Physics-Constrained Modeling of the Thermal Conductivity via Sequential Quadratic Programming Optimization in Nuclear Fusion Plasmas

by

Zachary Pelli

Presented to the Graduate and Research Committee of Lehigh University in Candidacy for the Degree of Master of Science

in

Mechanical Engineering

Lehigh University

Department of Mechanical Engineering and Mechanics

Bethlehem, PA 18015

August 05, 2016

Certificate of Approval

This thesis is accepted and approved in partial fulfillment of the requirements for the Master of Science in Mechanical Engineering.

August 05, 2016

Date

Professor Eugenio Schuster

Thesis Advisor

Professor Gary Harlow

Chairperson of Department

Acknowledgements

I would like to thank Professor Schuster for taking me on as a Master's candidate. His guidance was instrumental in my time pursuing this Master's degree, and I could not have learned as much without his constant help. I would like to thank PhD candidates Hexiang Wang and William Wehner, who provided help bringing me up to speed on the theory behind nuclear fusion as well as on the current state of technology in Lehigh's Plasma Control Laboratory.

I would also like to thank my family for their support, in particular my parents who gave me a loan to fund my MSc. studies.

Finally I would like to thank Cristina for her unrelenting support throughout this effort, and my good friend Joe for his help in the revision process.

Contents

List of Figures

Abstract

The plasma electron temperature (T_e) plays a critical role in a tokamak nuclear fusion reactor since temperatures on the order of 10^8K are required to achieve fusion conditions. Many plasma properties in a tokamak nuclear fusion reactor are modeled by partial differential equations (PDE's) because they depend not only on time but also on space. In particular, the dynamics of the electron temperature is governed by a PDE referred to as the Electron Heat Transport Equation (EHTE). In this work, a numerical method is developed to solve the EHTE based on a custom finite-difference technique. The solution of the EHTE is compared to temperature profiles obtained by using TRANSP, a sophisticated plasma transport code, for specific discharges from the DIII-D tokamak, located at the DIII-D National Fusion Facility in San Diego, CA.

The thermal conductivity (also called thermal diffusivity) of the electrons (χ_e) is a plasma parameter that plays a critical role in the EHTE since it indicates how the electron temperature diffusion varies across the minor effective radius of the tokamak. TRANSP approximates χ_e through a curve-fitting technique to match experimentally measured electron temperature profiles. While complex physics-based model have been proposed for χ_e, there is a lack of a simple mathematical model for the thermal diffusivity that could be used for control design. In this work, a model for χ_e is proposed based on a scaling law involving key plasma variables such as the electron temperature (T_e), the electron density (n_e), and the safety factor (q). An optimization algorithm is developed based on the Sequential Quadratic Programming (SQP) technique to optimize the scaling factors appearing in the proposed model so that the predicted electron temperature and magnetic flux profiles match predefined target profiles in the best possible way. A simulation study summarizing the outcomes of the optimization procedure is presented to illustrate the potential of the proposed modeling method.

Chapter 1

Introduction

1.1 Background to Fusion

In the past decades, nuclear fusion has risen as a viable alternative energy source to fossil fuels, and has been theorized to be more efficient and practical than wind, solar, and other forms of renewable energy. Particular advantages of nuclear fusion include its sustainability with current resources, its operation in a clean and safe manner, and its lack of dependency on favorable weather patterns.

Nuclear fusion is the process of combining two light atoms together to form a heavier atom, the byproduct of which are energetic particles ejected from the nucleus. The kinetic energy of these particles is captured and converted into usable electrical energy through a conventional Rankine cycle [1]. The hydrogen isotopes Deuterium (${}_1^2H$) and Tritium (${}_1^3H$) are typically the reactants due to their higher probability of fusion. The products of this fusion reaction are an α particle (${}_2^4He$) and an energetic neutron. In order to allow these reactants to fuse, the isotopes must posess enough kinetic energy to overcome the Coulombic repulsion force that exists between two positively charged nuclei. In a nuclear fusion reactor this is achieved by heating the fuel gas to temperatures on the order of 10^8 K so that the nuclei contain enough kinetic energy to fuse [1]. At these conditions, the Deuterium and Tritium gases become ionized to form a plasma.

Once in this plasma state, also know as the fourth state of matter, the challenge becomes confining the plasma within the reactor and sustaining the intense temperatures and pressures required for fusion. Fortunately, due to the ionization of its particles, the plasma can conduct electrical current and interact with magnetic fields. Therefore, magnetic confinement arises as a viable mechanism for containing the plasma within a given volume and preventing it from touching the inner walls of the tokamak vessel. In magnetic confinement, externally generated magnetic fields are generated to force the trajectories of both electrons and ions within the plasma by exploiting the resulting Lorentz force.

This work focuses on tokamaks, one of the most promising magnetic confinement devices where the magnetic field lines close in on themselves and form a torus. In a tokamak, the magnetic field lines are configured so that they follow a helical path through the torus, meaning they curve around in the poloidal direction (the poloidal angle is defined around the toroidal direction on a torus' cross section) as well as in the toroidal direction [1].

1.2 Spatial Coordinates of the Tokamak

The helical magnetic field ($\vec{B}$) in a tokamak plasma is made up of a toroidal component ($\vec{B}_\phi$) and a poloidal component ($\vec{B}_\theta$). Following any magnetic field line a number of times around the torus a magnetic flux surface is mapped, which marks points of constant poloidal magnetic flux (Ψ). A collection of such points along the plasma radial coordinate is called the poloidal magnetic flux profile [2]. The poloidal magnetic flux is defined as

$$\Psi = \int \vec{B}_\theta \cdot d\vec{A}_Z \tag{1.1}$$

where $\vec{A}_Z$ corresponds to a disk of radius R that is perpendicular to a unit vector in the z-direction [1]. Nested toroidal surfaces (as seen in Figure 1.1), called magnetic flux surfaces, are defined by a constant poloidal magnetic flux.

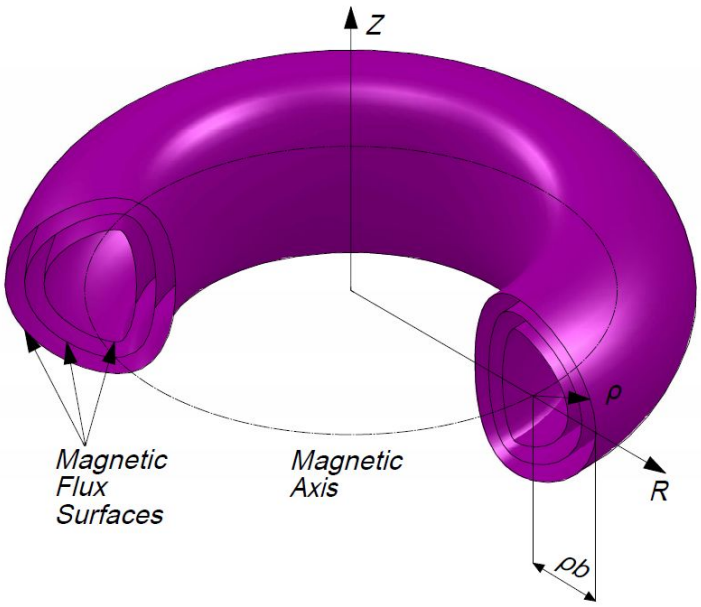

Figure 1.1: Schematic of tokamak with axes [4].

The major radial direction, or the direction from the center of the torus outwards, is defined as R, with the geometric major radius of the torus denoted as R_0. Due to the toroidal symmetry in the tokamak, we are interested in defining a

coordinate system for the two-dimensional poloidal cross section. Since the plasma properties are constant on the nested magnetic flux surfaces, the two-dimensional space can be reduced to a one-dimensional space by defining a spatial coordinate indexing the magnetic flux surfaces. In this case, we choose the mean effective minor radius ρ as the indexing variable, which is defined from the relationship

$$\Phi = \pi B_{\phi,0} \rho^2, \tag{1.2}$$

where Φ denote the toroidal magnetic flux and $B_{\phi,0}$ represents the toroidal magnetic field strength on the magnetic axis. This spatial coordinate can be normalized with respect to its value at the plasma boundary, i.e. the normalized mean effective minor radius $\hat{\rho}$ is defined as

$$\hat{\rho} = \frac{\rho}{\rho_b} \tag{1.3}$$

where ρ_b is the mean effective minor radius of the last closed magnetic flux surface (or boundary) [2].

A key property that is related to both the stability and performance of the plasma is the safety factor profile (q-profile) [3], which is related to both the poloidal magnetic flux in (1.1) and the toroidal magnetic flux in (1.2). The q-profile is defined as

$$q(\hat{\rho}, t) = -\frac{d\Phi}{d\Psi} = -\frac{B_{(\phi,0)} \rho_b^2 \hat{\rho}}{\partial \psi / \partial \hat{\rho}} \tag{1.4}$$

where t is the time and ψ is the poloidal stream function, which is closely related to the poloidal flux Ψ according to $\Psi = 2\pi\psi$.

The time evolution of plasma magnetic variables such as the poloidal magnetic flux Ψ and kinetic variables such as the electron temperature T_e must be modeled in tokamaks by using partial differential equations (PDE's) since these plasma properties depend not only on time but also on space. As explained above, these PDEs are one-dimensional with the chosen spatial coordinate $\hat{\rho}$.

1.3 Magnetic Diffusion Equation (MDE)

The evolution of the poloidal magnetic flux profile in a tokamak is modeled by the Magnetic (Flux) Diffusion Equation (MDE)

$$\frac{\partial \psi}{\partial t} = \frac{\eta(T_e)}{\mu_0 \rho_b^2 \hat{F}^2} \frac{1}{\hat{\rho}} \frac{\partial}{\partial \hat{\rho}} \left(\hat{\rho} \hat{F} \hat{G} \hat{H} \frac{\partial \psi}{\partial \hat{\rho}} \right) + R_0 \hat{H} \eta(T_e)[j_{aux} + j_{bs}] \tag{1.5}$$

where $\psi(\hat{\rho}, t)$ is the poloidal stream function, $T_e(\hat{\rho}, t)$ is the electron temperature, $\eta(\hat{\rho}, t)$ is the plasma resistivity profile, which is a function of $T_e(\hat{\rho}, t)$. The geometric spatial factors $\hat{F}(\hat{\rho}, t)$, $\hat{G}(\hat{\rho}, t)$, $\hat{H}(\hat{\rho}, t)$ are related to the magnetic configuration of a particular plasma MHD equilibrium [1] and μ_0 is the vacuum permeability (constant). The noninductive auxiliary current-drive and bootstrap current-drive sources are denoted by j_{aux} and j_{bs} respectively. The boundary conditions for the MDE are written as

$$\frac{\partial \Psi}{\partial \hat{\rho}}(0, t) = 0 \qquad \frac{\partial \Psi}{\partial \hat{\rho}}(1, t) = -k_{I_p} I_p(t) \tag{1.6}$$

where $I_p(t)$ is the total plasma current and k_{I_p} is a geometric constant. The boundary condition at $(\hat{\rho} = 0)$ indicates symmetry with respect to the magnetic axis.

1.4 Electron Heat Transport Equation (EHTE)

1.4.1 The EHTE

The electron kinetic energy at any spatial point and time can be modeled mathematically by a partial differential equation called the Electron Heat Transport Equation (EHTE). The EHTE in a tokamak is defined as

$$\frac{3}{2} \frac{\partial}{\partial t}[n_e T_e] = \frac{1}{\rho_b^2 \hat{H}} \frac{1}{\hat{\rho}} \frac{\partial}{\partial \hat{\rho}} [\hat{\rho} \frac{\hat{G} \hat{H}^2}{\hat{F}} (\chi_e n_e) \frac{\partial T_e}{\partial \hat{\rho}}] + Q_e \tag{1.7}$$

with boundary conditions

$$\frac{\partial T_e}{\partial \hat{\rho}}(0,t) = 0 \qquad\qquad T_e(1,t) = T_{e,boundary} \tag{1.8}$$

where any variable with the subscript (e) denotes a characteristic of the plasma electrons. According to standard nuclear fusion nomenclature, $n_e(\hat{\rho},t)$ represents the electron density, $T_e(\hat{\rho},t)$ is the electron temperature, $\hat{\rho}$ is the normalized effective minor radius, and ρ_b is the mean effective minor radius of the last closed magnetic flux surface. The geometric factors $\hat{F}(\hat{\rho},t)$, $\hat{G}(\hat{\rho},t)$, $\hat{H}(\hat{\rho},t)$ are profiles associated with the shape of the plasma within the tokamak. $Q_e(\hat{\rho},t)$ is the total heat added to the electrons, which is a combination of the electrocyclotron heating (ECH), neutral beam injection (NBI), ohmic heating (OH), and another sources. The variable χ_e in (1.7) denotes the thermal diffusivity.

1.4.2 Thermal Diffusivity χ_e

The location of the highest electron temperature and density occurs at the magnetic axis of the confined plasma. Very high temperature and density gradients develop between the magnetic axis ($\hat{\rho} = 0$) and the boundary of the plasma ($\hat{\rho} = 1$). In particular, the thermal diffusivity χ_e indicates how strongly the temperature diffuses at each spatial location and point in time. The thermal diffusivity may change dramatically through the duration of a discharge.

In analysis mode, sophisticated transport codes like TRANSP compute a χ_e evolution consistent with the experimentally measured temperature evolution. In predictive model, where experimental temperature measurements are not available, TRANSP uses complex theoretical models proposed for the thermal diffusivity. There is a lack, however, of a model simple enough to be used in control design.

1.5 Objective

Previous work by members of the Lehigh University Plasma Control Group includes a numerical solver for the MDE based on a hybrid finite difference technique. One of the goals of this thesis work is to extend this approach to the EHTE. By combining both explicit and implicit finite-difference techniques, a hybrid numerical solver is proposed for the EHTE in Chapter 2. The numerical solutions of the EHTE at different instants of time are compared with TRANSP-computed electron temperature profiles based on experimental measurements from the DIII-D shot 147634.

Another goal of this thesis work is the development of a control-oriented model for the thermal diffusivity χ_e. In Chapter 3 and Chapter 4, χ_e is modeled as a time-independent spatial function, while in Chapter 5 χ_e is modeled as a time-dependent scaling law involving three plasmas states, namely the electron temperature (T_e), the electron density (n_e), and the safety factor (q). The proposed model is written as

$$\chi_e = (T_e)^{\alpha}(n_e)^{\beta}(q)^{\gamma} \tag{1.9}$$

The values of χ_e at selected spatial points in Chapter 3 and Chapter 4, and the scaling factors α, β, and γ in Chapter 5, are determined by an optimization algorithm based on the Sequential Quadratic Programming (SQP) technique.

Chapter 2

Custom Finite Difference Solution to the EHTE

2.1 Finite Difference Techniques for Solving PDEs

2.1.1 Discrete System Indexing

As indicated before, the Electron Heat Transport Equation (EHTE) is a nonlinear partial differential equation. Thus a variety of numerical approaches can be taken to achieve its solution. Finite differentiation is an efficient method for the solution of PDEs that has been extensively studied [5]. The basic principle behind finite differentiation is to break down an infinite-dimensional system into a grid of both spatial and temporal points. In a Cartesian finite difference grid for a length L, the step size in the x-direction is Δx, with the node number defined as i. Given a total number of points N, we can identify the discretized nodes in the x-direction

$$x(i) = (i-1)\Delta x \qquad \text{where} \qquad \Delta x = \frac{\text{Total Length}}{\text{Number of points}} = \frac{L}{N-1} \tag{2.1}$$

Each individual location along the x coordinate will be

$$\begin{aligned} &i = 1, \quad x(1) = 0 \\ &i = 2, \quad x(2) = \Delta x \\ &i = 3, \quad x(3) = 2\Delta x \\ &\vdots \\ &i = N, \quad x(N) = (N-1)\Delta x = (N-1)\frac{L}{(N-1)} = L \end{aligned} \tag{2.2}$$

The exact same discretization can be applied in the Cartesian y-direction. Substituting the length L for a height H and substituting N for M results in the following nodes:

$$y(j) = (j-1)\Delta y \qquad \text{where} \qquad \Delta y = \frac{\text{Total Height}}{\text{Number of points}} = \frac{H}{M-1} \tag{2.3}$$

Individually, each location along the y coordinate will be

$$\begin{aligned} for \quad &j = 1, \quad y(1) = 0 \\ &j = 2, \quad y(2) = \Delta y \\ &j = 3, \quad y(3) = 2\Delta y \\ &\vdots \\ &j = M, \quad y(M) = (M-1)\Delta y = (M-1)\frac{H}{(M-1)} = H \end{aligned} \tag{2.4}$$

The plasma dynamics can then be indexed according to these discrete variables (i, j), where $\hat{\rho}$ plays the role of the x coordinate and t plays the role of the y coordinate. Thus, the electron temperature $T_e(\hat{\rho}_i, t_j)$ is equivalent to $T_e(i, j)$ in the discrete system, $n_e(\hat{\rho}_i, t_j)$ is equivalent to $n_e(i, j)$, and so forth. For simplicity, the (e) subscript is dropped from now on and the temporal node indicated in the superscript. Thus $T_e(i, j)$ is further reduced to T_i^j, where i denotes the nodal location on the spatial axis and j is the nodal location on the temporal axis.

2.1.2 Finite Difference Example

To illustrate the discretization process in a simplified example, we can examine the unsteady heat-conduction equation in (2.5). Note that this equation is not directly relevant to the solution of the EHTE, and is only being analyzed to demonstrate possible finite difference approaches.

$$\frac{\partial T}{\partial t} = \kappa \frac{\partial^2 T}{\partial x^2} \tag{2.5}$$

The equation above is known as the unsteady heat conduction equation, where T is the temperature, t and x are the temporal and spatial variables respectively, and κ is the thermal diffusivity of the material. Using the discrete index system from (2.1-2.2), T_i^j denotes the temperature at the spatial node i and the temporal node j. The equation can be forward discretized at the (i, j) point on the grid as

$$\begin{aligned} \left.\frac{\partial T}{\partial t}\right|_i^j &= \frac{T_i^{j+1} - T_i^j}{\Delta t} + O(\Delta t) \\ \left.\frac{\partial^2 T}{\partial x^2}\right|_i^j &= \frac{T_{i-1}^j - 2T_i^j + T_{i+1}^j}{2\Delta x} + O(\Delta x^2) \end{aligned} \tag{2.6}$$

The terms $O(\Delta t)$ and $O(\Delta x^2)$ are the error terms associated with the discretization, proportional to the time step and the square of the spatial step. As previously stated, i and j are the node numbers in each discrete dimension. Inserting (2.6) into (2.5) results in

$$\frac{T_i^{j+1} - T_i^j}{\Delta t} + O(\Delta t) = \kappa\Big(\frac{T_{i-1}^j - 2T_i^j + T_{i+1}^j}{2\Delta x}\Big) + O(\Delta x^2) \tag{2.7}$$

and rearranging for T_i^{j+1} yields

$$T_i^{j+1} \approx \kappa \Delta t\Big(\frac{T_{i-1}^j - 2T_i^j + T_{i+1}^j}{2\Delta x}\Big) + T_i^j \tag{2.8}$$

which provides T at time $j+1$ for the spatial node i as a function of T at time j at different spatial nodes.

The discrete finite difference technique employed in (2.8) is called the Explicit Forward-Temporal Central-Spatial Method, or Explicit FTCS Method. According to the Von Neumann stability analysis [6], the Explicit FTCS Method is conditionally stable, proportional to the temporal step Δt and inversely proportional to the spatial step Δx. While the FTCS Method is the simplest finite difference technique to implement, it requires a small Δt to maintain stability.

In an effort to reduce the dependency on the size of Δt and ensure stability, an implicit finite difference technique can be used. In the Implicit BTCS (Backwards-Temporal Central-Spatial) or Laasonen method, the PDE (2.5) can be discretized at time $j+1$ as

$$\left.\frac{\partial T}{\partial t}\right|_i^{j+1} = \kappa \left.\frac{\partial^2 T}{\partial x^2}\right|_i^{j+1} \tag{2.9}$$

Individually the components in (2.9) are discretized according the the BTCS method and represented as

$$\begin{aligned} \left.\frac{\partial T}{\partial t}\right|_i^{j+1} &\approx \frac{T_i^{j+1} - T_i^j}{\Delta t} \\ \left.\frac{\partial^2 T}{\partial x^2}\right|_i^{j+1} &\approx \frac{T_{i-1}^{j+1} - 2T_i^{j+1} + T_{i+1}^{j+1}}{2\Delta x} \end{aligned} \tag{2.10}$$

Replacing the expansions in (2.10) into (2.9) results in

$$\frac{T_i^{j+1} - T_i^j}{\Delta t} = \kappa\Big(\frac{T_{i-1}^{j+1} - 2T_i^{j+1} + T_{i+1}^{j+1}}{2\Delta x}\Big) \tag{2.11}$$

where T_i^j, κ, Δt, and Δx are known quantities. Note that unlike the explicit scenario, where we were able to rearrange for the single unknown T_i^{j+1}, the implicit method requires a system of equations to isolate the T_i^{j+1} component. Further expanding (2.11) and rearranging for the T^{j+1} term yields

$$T_i^{j+1}\left(1 + \frac{\kappa\Delta t}{\Delta x}\right) - T_{i-1}^{j+1}\left(\frac{\kappa\Delta t}{\Delta x}\right) - T_{i+1}^{j+1}\left(\frac{\kappa\Delta t}{\Delta x}\right) = T_i^j \tag{2.12}$$

Since the term $\frac{\kappa\Delta t}{\Delta x}$ is made up of all known variables, we can abbreviate the

constant as c_1. Equation (2.12) then becomes

$$T_i^{j+1}(1+c_1) - T_{i-1}^{j+1}(c_1) - T_{i+1}^{j+1}(c_1) = T_i^j \tag{2.13}$$

By combining (2.13) for $i = 1, \ldots, N$, together with the boundary conditions at $i = 1$ and $i = N$, we obtain a system of equations of the general form $Ax = b$, where

$$x = \begin{bmatrix} T_1^{j+1} \\ T_2^{j+1} \\ \vdots \\ T_N^{j+1} \end{bmatrix}, \qquad b = \begin{bmatrix} T_1^{j} \\ T_2^{j} \\ \vdots \\ T_N^{j} \end{bmatrix} \tag{2.14}$$

The Implicit BTCS method is *unconditionally stable* [6], however results in a system of equations that must be computed. For the unsteady heat conduction example, its solution is rather trivial because A is a constant matrix. However, for equations where the matrix A is not constant but a function of the state, computational requirements increase dramatically.

When a circumstance arises that requires the simplicity of the Explicit FTCS method with the stability of the Implicit BTCS method, a hybrid finite difference solution can be formulated. There is no preferred form when mathematically developing a hybrid solution, and so the user can choose how to manipulate the PDE depending on the data available and the desired simplicity of the model. For generating a solution of the Electron Heat Transport Equation, a custom hybrid finite difference solution is propose that combines the Implicit BTCS and Explicit FTCS methods.

2.2 Expanding the Electron Heat Transport Equation

The EHTE can be written as

$$\frac{3}{2}\frac{\partial}{\partial t}[nT] = \frac{1}{\rho_b^2 \hat{H}}\frac{1}{\hat{\rho}}\frac{\partial}{\partial \hat{\rho}}[\hat{\rho}\frac{\hat{G}\hat{H}^2}{\hat{F}}(\chi n)\frac{\partial T}{\partial \hat{\rho}}] + Q \tag{2.15}$$

where the (e) subscripts has been removed for simplicity. The boundary conditions are given by

$$\begin{aligned} \frac{\partial T}{\partial \hat{\rho}} &= 0 \quad at\ \ \hat{\rho} = 0 \\ T &= 0 \quad at\ \ \hat{\rho} = 1 \end{aligned} \tag{2.16}$$

The EHTE from (2.15) needs to be fully expanded before the different finite difference methods can be applied to the PDE. Equation (2.15) has two main components that can be expanded via the chain rule - to ease the solution process these two parts can be pulled out of the EHTE and expanded independently. The terms to be expanded are:

$$\frac{3}{2}\frac{\partial}{\partial t}[nT] \tag{2.17}$$

and

$$\frac{\partial}{\partial \hat{\rho}}[\hat{\rho}\frac{\hat{G}\hat{H}^2}{\hat{F}}(\chi n)\frac{\partial T}{\partial \hat{\rho}}] \tag{2.18}$$

Applying the chain rule to (2.17), we obtain

$$\frac{3}{2}\frac{\partial}{\partial t}[nT] = \frac{3}{2}\frac{\partial n}{\partial t}T + \frac{3}{2}\frac{\partial T}{\partial t}n \tag{2.19}$$

The expansion of (2.18) is more complex, but can be represented as

$$\frac{\partial}{\partial \hat{\rho}}\Big[\frac{\hat{\rho}\hat{G}\hat{H}^2\chi n}{\hat{F}}\frac{\partial T}{\partial \hat{\rho}}\Big] = \frac{\partial}{\partial \hat{\rho}}\Big[\frac{\hat{\rho}\hat{G}\hat{H}^2\chi n}{\hat{F}}\Big] * \Big[\frac{\partial T}{\partial \hat{\rho}}\Big] + \Big[\frac{\partial^2 T}{\partial \hat{\rho}^2}\Big] * \Big[\frac{\hat{\rho}\hat{G}\hat{H}^2\chi n}{\hat{F}}\Big] \tag{2.20}$$

Again the chain rule needs to be applied to the $\frac{\partial}{\partial \hat{\rho}}\Big[\frac{\hat{\rho}\hat{G}\hat{H}^2\chi n}{\hat{F}}\Big]$ term in (2.20), which

is expanded as

$$\frac{\partial}{\partial\hat{\rho}}\Big[\frac{\hat{\rho}\hat{G}\hat{H}^2\chi n}{\hat{F}}\Big] = \Big[\frac{\hat{G}\hat{H}^2\chi n}{\hat{F}} + \Big(\frac{\partial G}{\partial\hat{\rho}}\Big)\frac{\hat{\rho}\hat{H}^2\chi n}{\hat{F}} + \Big(\frac{2\partial\hat{H}}{\partial\hat{\rho}}\Big)\frac{\hat{\rho}\hat{G}\chi n}{\hat{F}} + \Big(\frac{\partial\chi}{\partial\hat{\rho}}\Big)\frac{\hat{\rho}\hat{G}\hat{H}^2 n}{\hat{F}} + \Big(\frac{\partial n}{\partial\hat{\rho}}\Big)\frac{\hat{\rho}\hat{G}\hat{H}^2\chi}{\hat{F}} - \Big(\frac{\partial F}{\partial\hat{\rho}}\Big)\frac{\hat{\rho}\hat{G}\hat{H}^2\chi n}{\hat{F}^2}\Big] \tag{2.21}$$

Plugging (2.21) back into (2.20), the result to the chain rule expansion of (2.18) is expressed as

$$\frac{\partial}{\partial\hat{\rho}}\Big[\frac{\hat{\rho}\hat{G}\hat{H}^2\chi n}{\hat{F}}\frac{\partial T}{\partial\hat{\rho}}\Big] = \Big[\frac{\hat{G}\hat{H}^2\chi n}{\hat{F}} + \Big(\frac{\partial G}{\partial\hat{\rho}}\Big)\frac{\hat{\rho}\hat{H}^2\chi n}{\hat{F}} + \Big(\frac{2\partial\hat{H}}{\partial\hat{\rho}}\Big)\frac{\hat{\rho}\hat{G}\chi n}{\hat{F}} + \Big(\frac{\partial\chi}{\partial\hat{\rho}}\Big)\frac{\hat{\rho}\hat{G}\hat{H}^2 n}{\hat{F}} + \Big(\frac{\partial n}{\partial\hat{\rho}}\Big)\frac{\hat{\rho}\hat{G}\hat{H}^2\chi}{\hat{F}} - \Big(\frac{\partial F}{\partial\hat{\rho}}\Big)\frac{\hat{\rho}\hat{G}\hat{H}^2\chi n}{\hat{F}^2}\Big] * \Big[\frac{\partial T}{\partial\hat{\rho}}\Big] + \Big[\frac{\hat{\rho}\hat{G}\hat{H}^2\chi n}{\hat{F}}\Big] * \Big[\frac{\partial^2 T}{\partial\hat{\rho}^2}\Big] \tag{2.22}$$

Finally, we can bring the two expansions of (2.17) and (2.18) back into the EHTE to obtain

$$\begin{aligned}\frac{3}{2}\frac{\partial n}{\partial t}T + \frac{3}{2}\frac{\partial T}{\partial t}n = \frac{1}{\rho_b^2\hat{H}\hat{\rho}}\Bigg\{&\Big[\frac{\hat{G}\hat{H}^2\chi n}{\hat{F}} + \Big(\frac{\partial G}{\partial\hat{\rho}}\Big)\frac{\hat{\rho}\hat{H}^2\chi n}{\hat{F}} + \Big(\frac{2\partial\hat{H}}{\partial\hat{\rho}}\Big)\frac{\hat{\rho}\hat{G}\chi n}{\hat{F}} \\ &+ \Big(\frac{\partial\chi}{\partial\hat{\rho}}\Big)\frac{\hat{\rho}\hat{G}\hat{H}^2 n}{\hat{F}} + \Big(\frac{\partial n}{\partial\hat{\rho}}\Big)\frac{\hat{\rho}\hat{G}\hat{H}^2\chi}{\hat{F}} - \Big(\frac{\partial F}{\partial\hat{\rho}}\Big)\frac{\hat{\rho}\hat{G}\hat{H}^2\chi n}{\hat{F}^2}\Big] * \Big[\frac{\partial T}{\partial\hat{\rho}}\Big] \\ &+ \Big[\frac{\hat{\rho}\hat{G}\hat{H}^2\chi n}{\hat{F}}\Big] * \Big[\frac{\partial^2 T}{\partial\hat{\rho}^2}\Big]\Bigg\} + Q\end{aligned} \tag{2.23}$$

By defining

$$f_1 = \Big(\frac{\hat{\rho}\hat{G}\hat{H}^2\chi n}{\hat{F}}\Big)\frac{1}{\rho_b^2 H\hat{\rho}} \tag{2.24}$$

$$\begin{aligned}f_2 = \frac{1}{\rho_b^2\hat{H}\hat{\rho}}\Bigg\{&\Big[\frac{\hat{G}\hat{H}^2\chi n}{\hat{F}} + \frac{\partial G}{\partial\hat{\rho}}\Big(\frac{\hat{\rho}\hat{H}^2\chi n}{\hat{F}}\Big) + \frac{2\partial\hat{H}}{\partial\hat{\rho}}\Big(\frac{\hat{\rho}\hat{G}\chi n}{\hat{F}}\Big) \\ &+ \frac{\partial\chi}{\partial\hat{\rho}}\Big(\frac{\hat{\rho}\hat{G}\hat{H}^2 n}{\hat{F}}\Big) + \frac{\partial n}{\partial\hat{\rho}}\Big(\frac{\hat{\rho}\hat{G}\hat{H}^2\chi}{\hat{F}}\Big) - \frac{\partial F}{\partial\hat{\rho}}\Big(\frac{\hat{\rho}\hat{G}\hat{H}^2\chi n}{\hat{F}^2}\Big)\Big]\Bigg\}\end{aligned} \tag{2.25}$$

the EHTE can be rewritten simply as

$$\frac{3}{2}\frac{\partial n}{\partial t}T + \frac{3}{2}\frac{\partial T}{\partial t}n = f_1\frac{\partial^2 T}{\partial\hat{\rho}^2} + f_2\frac{\partial T}{\partial\hat{\rho}} + Q \tag{2.26}$$

2.3 Explicit FTCS Solution to the EHTE

2.3.1 Discretizing the EHTE According to Explicit FCTS

Now that sufficient background has been given to finite difference methods using the unsteady heat-conduction equation as an example, and the EHTE has been properly expanded to a form that is readily available for finite differencing, the Explicit FTCS solution to the EHTE is developed. Note from Section 2.1.2 that the Explicit FTCS method is only conditionally stable. In the Explicit FTCS method for the Electron Heat Transport Equation, the PDE is evaluated at the current time and solved to predict the future electron temperature. The components of the EHTE are written at (i, j) as

$$\begin{aligned}
&\left.\frac{\partial T}{\partial t}\right|_i^j = \frac{T_i^{j+1} - T_i^j}{\Delta t} \qquad n_i^j = n^{prof}(\rho_i) u_n(t_j) \qquad \left.\frac{\partial n}{\partial t}\right|_i^j = n^{prof}(\rho_i)\dot{u}_n(t_j) \\
&\left.\frac{\partial T}{\partial \hat{\rho}}\right|_i^j = \frac{T_{i+1}^j - T_{i-1}^j}{2\Delta\hat{\rho}} \qquad \left.\frac{\partial^2 T}{\partial \hat{\rho}^2}\right|_i^j = \frac{T_{i-1}^j - 2T_i^j + T_{i+1}^j}{\Delta\hat{\rho}^2} \qquad \left.\frac{\partial \chi}{\partial \hat{\rho}}\right|_i^j = \frac{\chi_{i+1}^j - \chi_i^j}{\Delta\hat{\rho}} \\
&\left.\frac{\partial F}{\partial \hat{\rho}}\right|_i^j = \frac{F_{i+1}^j - F_i^j}{\Delta\hat{\rho}} \qquad \left.\frac{\partial G}{\partial \hat{\rho}}\right|_i^j = \frac{G_{i+1}^j - G_i^j}{\Delta\hat{\rho}} \qquad \left.\frac{\partial H}{\partial \hat{\rho}}\right|_i^j = \frac{H_{i+1}^j - H_i^j}{\Delta\hat{\rho}}
\end{aligned} \tag{2.27}$$

Replacing the terms in (2.26) into the expanded EHTE (2.23), we arrive at the general Explicit FTCS form of the EHTE, i.e.

$$\begin{aligned}
\frac{3}{2}\left.\frac{\partial n}{\partial t}\right|_i^j T_i^j + \frac{3n_i^j}{2}\left(\frac{T_i^{j+1} - T_i^j}{\Delta t}\right) = \frac{1}{\rho_b^2 \hat{H}_i^j \hat{\rho}_i}\Bigg\{ &\left[\frac{\hat{G}_i^j \hat{H_i^j}^2 \chi_i^j n_i^j}{\hat{F}_i^j} + \left(\frac{\partial G}{\partial \hat{\rho}}\right)\Bigg|_i^j \frac{\hat{\rho}_i \hat{H_i^j}^2 \chi_i^j n_i^j}{\hat{F}_i^j}\right. \\
&+ \left(\frac{2\partial \hat{H}}{\partial \hat{\rho}}\right)\Bigg|_i^j \frac{\hat{\rho}_i \hat{G}_i^j \chi_i^j n_i^j}{\hat{F}_i^j} + \left(\frac{\partial \chi}{\partial \hat{\rho}}\right)\Bigg|_i^j \frac{\hat{\rho}_i \hat{G}_i^j \hat{H_i^j}^2 n_i^j}{\hat{F}_i^j} + \left(\frac{\partial n}{\partial \hat{\rho}}\right)\Bigg|_i^j \frac{\hat{\rho}_i \hat{G}_i^j \hat{H_i^j}^2 \chi_i^j}{\hat{F}_i^j} \\
&- \left(\frac{\partial F}{\partial \hat{\rho}}\right)\Bigg|_i^j \left.\frac{\hat{\rho}_i \hat{G}_i^j \hat{H_i^j}^2 \chi_i^j n_i^j}{\hat{F_i^j}^2}\right] * \left(\frac{T_{i+1}^j - T_{i-1}^j}{2\Delta\hat{\rho}}\right) + \left[\frac{\hat{\rho}_i \hat{G}_i^j \hat{H_i^j}^2 \chi_i^j n_i^j}{\hat{F}_i^j}\right] \\
&\left. * \left(\frac{T_{i-1}^j - 2T_i^j + T_{i+1}^j}{\Delta\hat{\rho}^2}\right)\right\} + Q_i^j
\end{aligned} \tag{2.28}$$

from which we can solve for T_i^{j+1}. Recall that the time step Δt has a significant effect on the stability of the solution, so an appropriate Δt must be selected.

2.3.2 The CFL condition

The Courant-Friedrichs-Lewy (CFL) condition is used as a stability check for explicit finite difference applications. The condition states that, given a space discretization, a time step bigger than some computable quantity should not be taken [7]. In essence this means that the time step must be kept small enough so that information has enough time to propogate through the space discretization [8]. The condition was developed by Richard Courant, Kurt Friedrichs, and Hans Lewy in 1928. Specifically made for analyzing the solving potential of explicit finite difference techniques, the equation assigns a constant to the relationship between the chosen time step and the theoretical best-value time step [7]. Mathematically this is represented by

$$CFL = \frac{u\Delta t}{\Delta x} \leq C_{max} \tag{2.29}$$

where C_{max} is 1 for explicit methods. In (2.28), Δx corresponds to the spatial grid step, which in our case is $\Delta\hat{\rho}$. The term u refers to the magnitude of the velocity, given in a length/time format.

2.3.3 Explicit Solution of the EHTE

The Explicit FTCS model for the Electron Heat Transport Equation was evaluated with three different time steps: $\Delta t = 0.01s$, $\Delta t = 0.001s$, and $\Delta t = 0.0001s$. The explicit model was set up according to the finite difference solution for the EHTE in (2.28), and data from DIII-D shot 147634 was used. This data included time-varying profiles for the geometric factors, electron temperature, density, and thermal diffusivity. The results of these simulations are displayed in Figure 2.1.

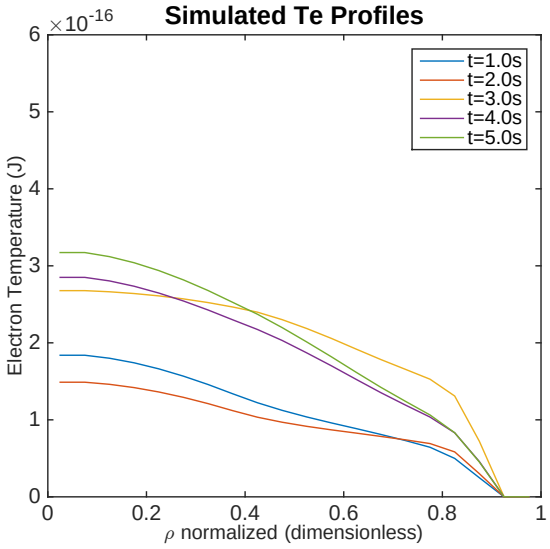

(a)

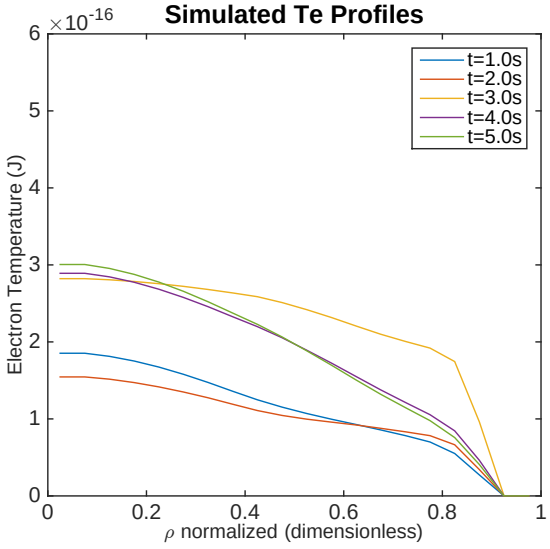

(b)

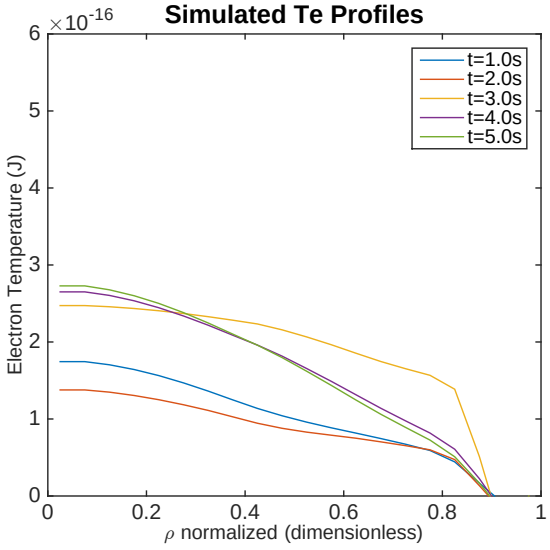

(c)

Figure 2.1: Explicit finite difference solution of the EHTE with (a) $\Delta t = 0.01s$, (b) $\Delta t = 0.001s$, and (c) $\Delta t = 0.0001s$.

From Figure 2.1 it appears that the high confinement H-mode pedestal, represented by the sharp drop in temperature near the plasma boundary, is only properly displayed for a higher mesh refinement. Particularly for $0 \leq t \leq 3.0$, the shapes of the profiles differ more between $\Delta t = 0.01s$ and $\Delta t = 0.001s$ than from $\Delta t = 0.001s$ and $\Delta t = 0.0001s$. Although not depicted, the EHTE was solved with an even greater mesh refinement but produced no noticeable difference from the results in Figure 2.1(c), denoting a convergence in accuracy.

2.4 Implicit BTCS Solution to the EHTE

As was shown in section 2.3, the Explicit FTCS method for the finite difference of the EHTE is highly restricted by the time step. We now wish to explore a technique that provides unconditional stability, regardless of temporal mesh refinement. Following the process set forth in section 2.1 for implicit discretization, we can apply the Implicit BTCS method to the Electron Heat Transport Equation. By discretizing the PDE at time $(j+1)$, we can write

$$\begin{aligned}
&\left.\frac{\partial T}{\partial t}\right|_i^{j+1} = \frac{T_i^{j+1} - T_i^j}{\Delta t} \qquad n_i^{j+1} = n^{prof}(\rho_i) u_n(t_{j+1}) \qquad \left.\frac{\partial n}{\partial t}\right|_i^{j+1} = n^{prof}(\rho_i)\dot{u}_n(t_{j+1}) \\
&\left.\frac{\partial T}{\partial \hat{\rho}}\right|_i^{j+1} = \frac{T_{i+1}^{j+1} - T_{i-1}^{j+1}}{2\Delta\hat{\rho}} \qquad \left.\frac{\partial^2 T}{\partial \hat{\rho}^2}\right|_i^{j+1} = \frac{T_{i-1}^{j+1} - 2T_i^{j+1} + T_{i+1}^{j+1}}{\Delta\hat{\rho}^2} \\
&\left.\frac{\partial \chi}{\partial \hat{\rho}}\right|_i^{j+1} = \frac{\chi_{i+1}^{j+1} - \chi_i^{j+1}}{\Delta\hat{\rho}} \qquad \left.\frac{\partial F}{\partial \hat{\rho}}\right|_i^{j+1} = \frac{F_{i+1}^{j+1} - F_i^{j+1}}{\Delta\hat{\rho}} \\
&\left.\frac{\partial G}{\partial \hat{\rho}}\right|_i^{j+1} = \frac{G_{i+1}^{j+1} - G_i^{j+1}}{\Delta\hat{\rho}} \qquad \left.\frac{\partial H}{\partial \hat{\rho}}\right|_i^{j+1} = \frac{H_{i+1}^{j+1} - H_i^{j+1}}{\Delta\hat{\rho}}
\end{aligned} \tag{2.30}$$

which yields

$$\begin{aligned}\frac{3}{2}\frac{\partial n}{\partial t}\bigg|_i^{j+1} T_i^{j+1} + \frac{3n_i^{j+1}}{2}\Big(\frac{T_i^{j+1}-T_i^j}{\Delta t}\Big) = \frac{1}{\rho_b^2 \hat{H}_i^{j+1}\hat{\rho}_i}\Bigg\{\Bigg[\Big(\frac{\hat{G}\hat{H}^2\chi n}{\hat{F}}\Big)\bigg|_i^{j+1} \\ + \frac{\partial G}{\partial\hat{\rho}}\bigg|_i^{j+1}\Big(\frac{\hat{\rho}\hat{H}^2\chi n}{\hat{F}}\Big)\bigg|_i^{j+1} + \frac{2\partial H}{\partial\hat{\rho}}\bigg|_i^{j+1}\Big(\frac{\hat{\rho}\hat{G}\chi\ n}{\hat{F}}\Big)\bigg|_i^{j+1} \\ + \frac{\partial \chi}{\partial\hat{\rho}}\bigg|_i^{j+1}\Big(\frac{\hat{\rho}_i\hat{G}\hat{H}^2 n}{\hat{F}}\Big)\bigg|_i^{j+1} + \frac{\partial n}{\partial\hat{\rho}}\bigg|_i^{j+1}\Big(\frac{\hat{\rho}\hat{G}\hat{H}^2\chi}{\hat{F}}\Big)\bigg|_i^{j+1} \\ - \frac{\partial F}{\partial\hat{\rho}}\bigg|_i^{j+1}\Big(\frac{\hat{\rho}\hat{G}\hat{H}^2\chi n}{\hat{F}^2}\Big)\bigg|_i^{j+1}\Bigg] * \Big(\frac{T_{i+1}^{j+1}-T_{i-1}^{j+1}}{2\Delta\hat{\rho}}\Big) + \Big(\frac{\hat{\rho}\hat{G}\hat{H}^2\chi n}{\hat{F}}\Big)\bigg|_i^{j+1} \\ * \Big(\frac{T_{i-1}^{j+1}-2T_i^{j+1}+T_{i+1}^{j+1}}{\Delta\hat{\rho}^2}\Big)\Bigg\} + Q_i^{j+1}\end{aligned} \tag{2.31}$$

Equation (2.31) can be rewritten as

$$\begin{aligned}T_{i+1}^{j+1}\Big(-\frac{f_1\big|_i^{j+1}}{\Delta\hat{\rho}^2} - \frac{f_2\big|_i^{j+1}}{2\Delta\hat{\rho}}\Big) + T_{i-1}^{j+1}\Big(-\frac{f_1\big|_i^{j+1}}{\Delta\hat{\rho}^2} + \frac{f_2\big|_i^{j+1}}{2\Delta\hat{\rho}}\Big) \\ + T_i^{j+1}\Big(\frac{3}{2}\frac{n_i^{j+1}}{\Delta t} + \frac{2f_1\big|_i^{j+1}}{\Delta\hat{\rho}^2}\Big) = f_3\big|_i^{j+1}T_i^j + Q_i^{j+1}\end{aligned} \tag{2.32}$$

where we have defined

$$f_3 = \frac{3}{2}\Big(\frac{n}{\Delta t} - \frac{\partial n}{\partial t}\Big) \tag{2.33}$$

The solution of equation (2.32) for T_i^{j+1} requires knowledge of $\hat{F}$, $\hat{G}$, $\hat{H}$, n (and its time derivative), χ, and Q at time $j+1$. However, this is not always the case. To avoid requiring knowledge of these plasma parameters at the future time $j+1$, we propose a hybrid method that retains the stability properties of the implicit method while keeping the computation simplicity of the explicit method.

2.5 Custom Hybrid Finite Difference Solution to the EHTE

Hybrid finite difference techniques are frequently implemented in engineering as a solution to complex PDEs, whether in fluid dynamics, heat and mass transfer,

or nuclear fusion. While standard hybrid equations such as the Crank-Nicolson method are commonplace for simple PDEs, we propose a custom version for the EHTE. For this hybrid model of the EHTE, we have chosen to implicitly discretize the temperature terms, while evaluating the rest of components of the equation at time j. Therefore, (2.32) is rewritten as

$$\begin{aligned} T_{i+1}^{j+1}\Big(-\frac{f_1\big|_i^j}{\Delta\hat{\rho}^2} - \frac{f_2\big|_i^j}{2\Delta\hat{\rho}}\Big) + T_{i-1}^{j+1}\Big(-\frac{f_1\big|_i^j}{\Delta\hat{\rho}^2} + \frac{f_2\big|_i^j}{2\Delta\hat{\rho}}\Big) \\ + T_i^{j+1}\Big(\frac{3}{2}\frac{n_i^{j+1}}{\Delta t} + \frac{2f_1\big|_i^j}{\Delta\hat{\rho}^2}\Big) = f_3\big|_i^j T_i^j + Q_i^j \end{aligned} \tag{2.34}$$

By evaluating (2.34) at $i = 2, \ldots, N-1$, and incorporating the boundary conditions at $i = 1$ and $i = N$, we obtain a linear system of equations. By defining

$$\begin{aligned} a_{i-1} &= \Big(-\frac{f_1}{\Delta\hat{\rho}^2} + \frac{f_2}{2\Delta\hat{\rho}}\Big)\Big|_i^j \\ a_i &= \Big(\frac{3}{2}\frac{n}{\Delta t} + \frac{2f_1}{\Delta\hat{\rho}^2}\Big)\Big|_i^j \\ a_{i+1} &= \Big(-\frac{f_1}{\Delta\hat{\rho}^2} - \frac{f_2}{2\Delta\hat{\rho}}\Big)\Big|_i^j \end{aligned} \tag{2.35}$$

for $2 \le i \le N-1$, the system of equations can be written as

$$[A]\begin{bmatrix} T_1^{j+1} \\ T_2^{j+1} \\ T_3^{j+1} \\ \vdots \\ T_{N-2}^{j+1} \\ T_{N-1}^{j+1} \\ T_N^{j+1} \end{bmatrix} = \begin{bmatrix} 0 \\ f_3\Big|_2^j T_2^j + Q_2^j \\ f_3\Big|_3^j T_3^j + Q_3^j \\ \vdots \\ f_3\Big|_{N-2}^j T_{N-2}^j + Q_{N-2}^j \\ f_3\Big|_{N-1}^j T_{N-1}^j + Q_{N-1}^j \\ 0 \end{bmatrix} \tag{2.36}$$

$$A = \begin{bmatrix} -3 & 4 & -1 & ... & 0 & 0 & 0 \\ a_1^{j+1} & a_2^{j+1} & a_3^{j+1} & ... & 0 & 0 & 0 \\ 0 & a_2^{j+1} & a_3^{j+1} & a_4^{j+1} & ... & 0 & 0 \\ \vdots & \vdots & \vdots & \vdots & \vdots & \vdots & \vdots \\ 0 & 0 & ... & a_{n-3}^{j+1} & a_{n-2}^{j+1} & a_{n-1}^{j+1} & 0 \\ 0 & 0 & 0 & ... & a_{n-2}^{j+1} & a_{n-1}^{j+1} & a_n^{j+1} \\ 0 & 0 & 0 & ... & 0 & 0 & 1 \end{bmatrix} \tag{2.37}$$

The first and last rows of the matrix A come from the discretized version of the boundary conditions, i.e.,

$$\begin{aligned} \left.\frac{\partial T}{\partial \hat{\rho}}\right|_1^{j+1} &= \frac{-3T_1^{j+1} + 4T_2^{j+1} - T_3^{j+1}}{2\Delta\hat{\rho}} = 0 \\ T_N^{j+1} &= 0 \end{aligned} \tag{2.38}$$

In the center of the plasma, where the plasma is most dense and the external heat sources are focused, the temperature is the highest. In turn, any direction away from this central peak will result in a negative gradient as the temperature diffuses to the boundary wall. This is captured by the first line in (2.38). The temperature at $\hat{\rho} = 1$ can be assumed to be zero or nearly zero. This is shown in the second line of (2.38).

2.6 DIII-D Tokamak Shot Parameters

With the hybrid finite difference scheme developed and applied to the EHTE, its prediction capability is now compared to TRANSP simulations. In order to carry out the comparison, all plasma data ($\hat{F}$, $\hat{G}$, $\hat{H}$, n (and its time derivative), χ, Q) was retrieved from TRANSP. This data corresponds to DIII-D shot 147634. The geometric factors $\hat{G}, \hat{H}$, and $\hat{F}$ from TRANSP are time varying profiles, as can be seen in Figure 2.2. However, the magnitude of the profiles undergo little deviation over the course of the shot, on the order of less than 10%.

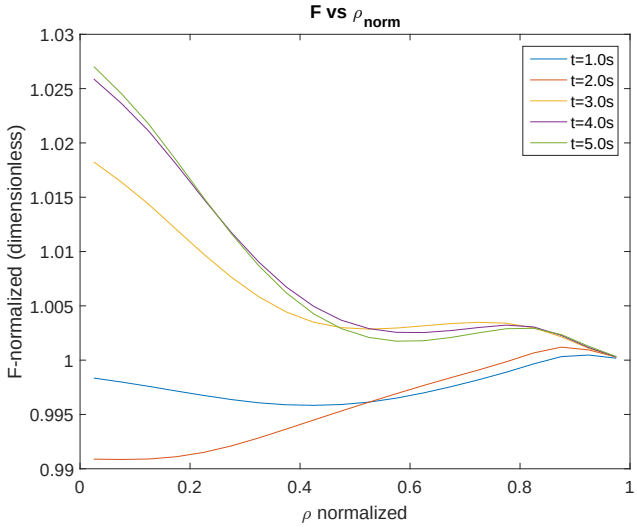

(a)

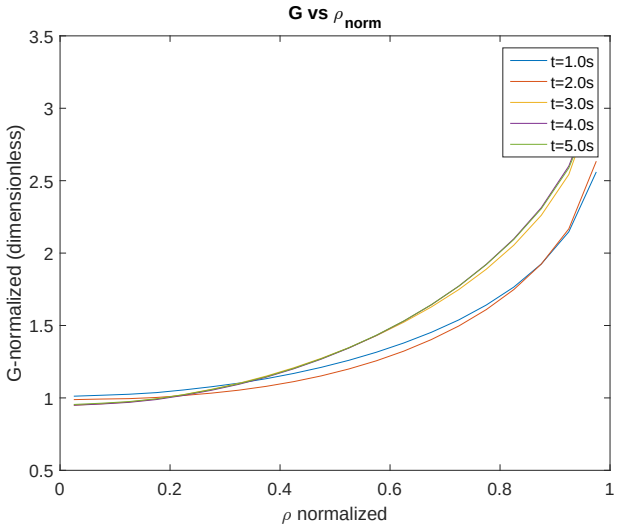

(b)

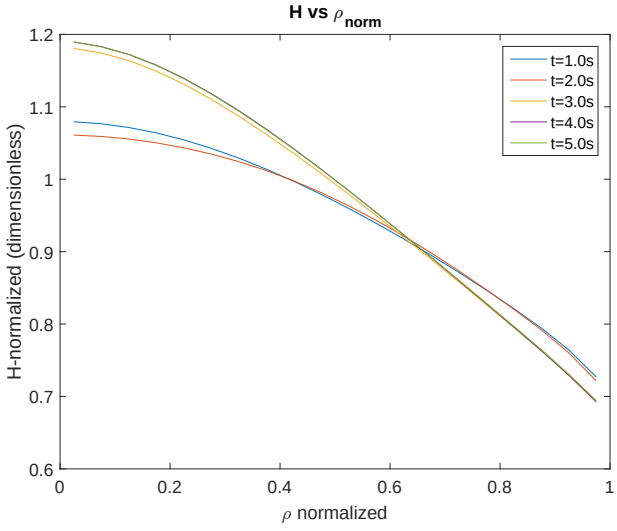

(c)

Figure 2.2: DIII-D tokamak geometric factors extracted from TRANSP: (a) $\hat{F}(\hat{\rho}, t)$, (b) $\hat{G}(\hat{\rho}, t)$, (c) $\hat{H}(\hat{\rho}, t)$.

The electron density has a similar shape to the temperature, with the peak density located at the center of the plasma and a sharp drop near the boundary from $0.8 \leq \hat{\rho} \leq 1$. This electron density profile is exhibited in Figure 2.3.

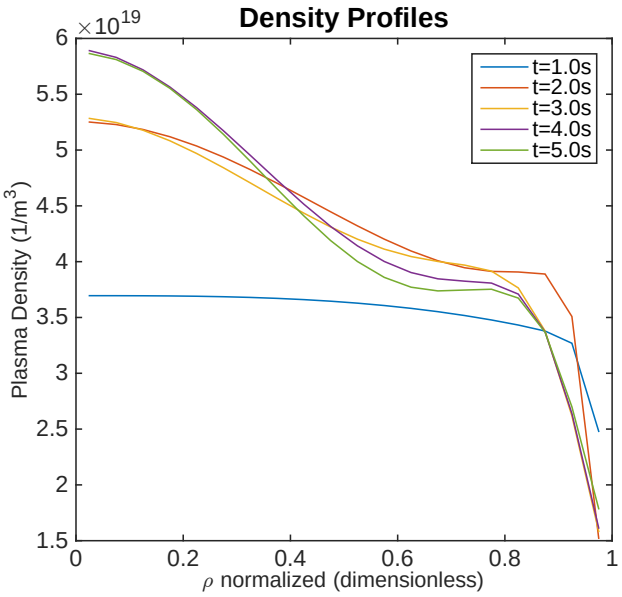

Figure 2.3: Electron density profiles at select times across the minor tokamak radius. Total shot time is 5.5 seconds.

As the plasma moves away from the $\hat{\rho} = 0$ (the center), the plasma slowly becomes less dense. However, an interesting phenomenom occurs near $\hat{\rho} = 0.9$ - the density plummets. This is known as the **H-mode pedestal**. "The high-confinement (H-mode) temperature and density pedestal is produced by a transport barrier characterized by a narrow, sharply defined region of steep temperature and density gradients. This pedestal is located near the last closed magnetic flux surface and typically extends over with a width of less that 5-10% of the plasma minor radius" [9]. This implies that as the plasma crosses the final magnetic flux surface, the temperature and density diffuse rapidly due to the massive gradients at the boundary. The H-mode pedestal's exclusive shape is characteristic only of high-confinement modes, making it a good benchmark to compare the accuracy of the EHTE solver since the pedestal must be present in our simulation results.

One of the greatest influences on the development of the electron temperature profile in both magnitude and shape are the heating sources. The external and

internal heating sources captured by the proposed model are the electrocyclotron heating, the neutral beam injection heating, and the resistance ohmic heating. This is represented by the equation in (2.39) below.

$$Q_e = Q_{NBIs} + Q_{ECE} + Q_{ohmic} \tag{2.39}$$

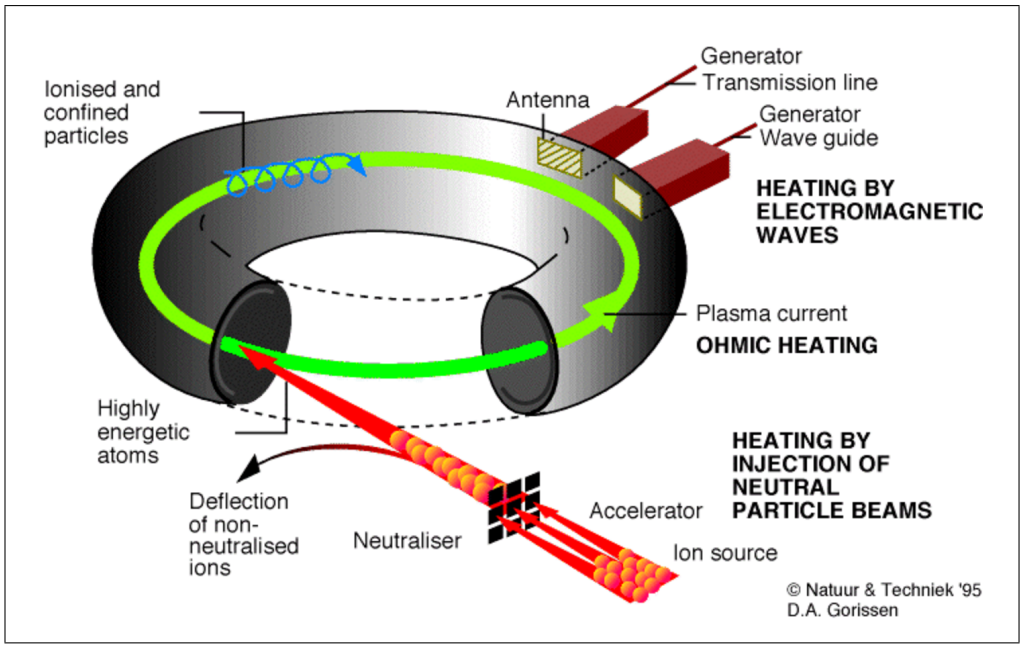

Figure 2.4: Graphic of heating sources for ITER [11].

These sources are graphically represented in Figure 2.4. The external heating is provided by two mechanisms. Electron Cyclotron Resonance Heating (ECRH) heats the electrons in the plasma with high intensity electromagnetic waves at the resonant frequency of the electrons. The electron cyclotron heating system is used to deposit heat in very specific places in the plasma, as a mechanism to minimize the build-up of certain instabilities that lead to cooling of the plasma [10]. The neutral beam injectors (NBIs) shoot neutrally charged particles into the plasma. Since these particles have no charge, they are not restricted by the magnetic field. However, they do collide with electrons and protons in the mix, transferring their kinetic energy and increasing the plasma temperature. The NBIs are positioned around the plasma at 4 different positions in DIIII-D: 30L/R, 150L/R, 210L/R,

330L/R. The number of the NBI corresponds to the orientation around the 360 degree tokamak that the NBI injectors are located at. The 210L/R location is oriented against the rotational flow of the plasma for experimental reasons. However for shot 147634, the 210L/R beams were not activated ($Q_{NBI_{210}} = 0$). The ECE and NBI heat sources are represented by the profiles plotted in Figure 2.5. Since both the EC and NBI heating systems are composed of several gyrotrons and injectors, respectively, the profiles in Figure 2.5 show the sources summed together. In other words, $Q_{ECE} = Q_{EC1} + Q_{EC2} + Q_{EC3} + Q_{EC4} + Q_{EC5} + Q_{EC6}$, $Q_{NBI} = Q_{nbi30L} + Q_{nbi30R} + Q_{nbi150L} + Q_{nbi150R} + Q_{nbi210L} + Q_{nbi210R} + Q_{nbi330L} + Q_{nbi330R}$.

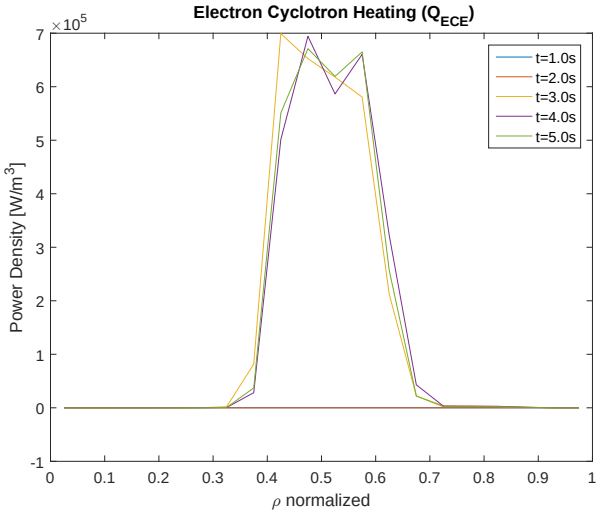

(a) ECE Heating Density Profiles at select times

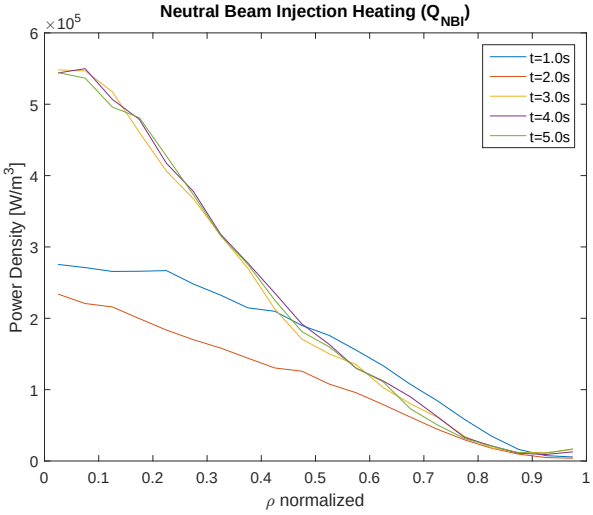

(b) NBI Heating Density Profiles at select times

Figure 2.5: External heating sources for shot 147634.

While Figure 2.5 clearly displays the magnitude of the ECEs and NBIs, more detail can be provided for the time-varying aspecst of the heat sources. In particular, the gyrotrons are not turned on until about 2 seconds in shot 147634. This is better represented in Figure 2.6, where it is clear how the external heat changes over the timespan of the shot. Due to the spike in the heat source after 2 seconds, we should expect to see that the electron temperature profiles grow correspondingly.

In addition to the external heat sources Q_{NBI} and Q_{ECE}, there is an internal source of heat denoted by the third term of (2.42). An induced current is used to provide the poloidal magnetic field in the reactor. The ionized plasma particles act as a resistor, converting some of this induced electrical power into heat. In tokamak nomeclature, this is known as ohmic heating (Q_{ohmic}). Ohmic heating is limited by two factors: Firstly the plasma current is induced via transformer action, which employs an increasing magnetic field. It is therefore pulsed and does not allow continuous plasma operation. Secondly the electric resistance, which produces the heat, decreases with the plasma temperature [12]. The time-varying ohmic heating density profiles are represented in Figure 2.7.

The final plasma parameter necessary to test the EHTE solver is the thermal diffusivity χ_e. As discussed in section 1.4.2, the thermal diffusivity in TRANSP is calculated by curve-fitting the predictive temperature profile to experimental data. The χ_e profile used in the simulations is shown in Figure 2.8. Note that for the entire duration of the shot, there is a sharp drop and then rise at $\hat{\rho} = 0.9$. This is evidence of the H-mode pedestal and is crucial to the development of the electron temperature in our model.

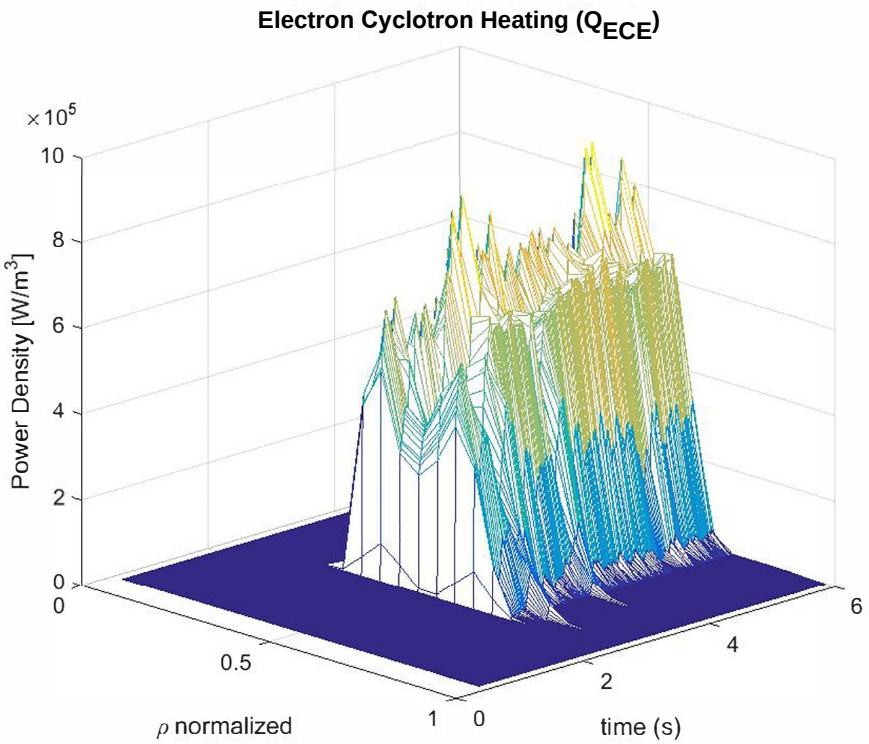

(a) ECE Heating Density Profiles for entire shot

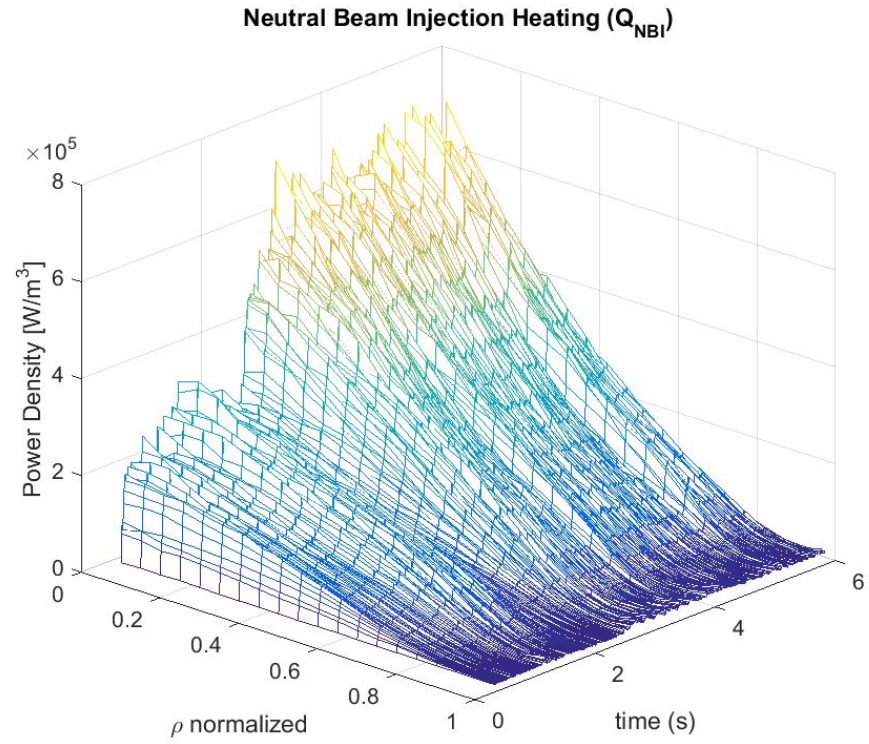

(b) NBI Heating Density Profiles for entire shot

Figure 2.6: External heating sources for shot 147634.

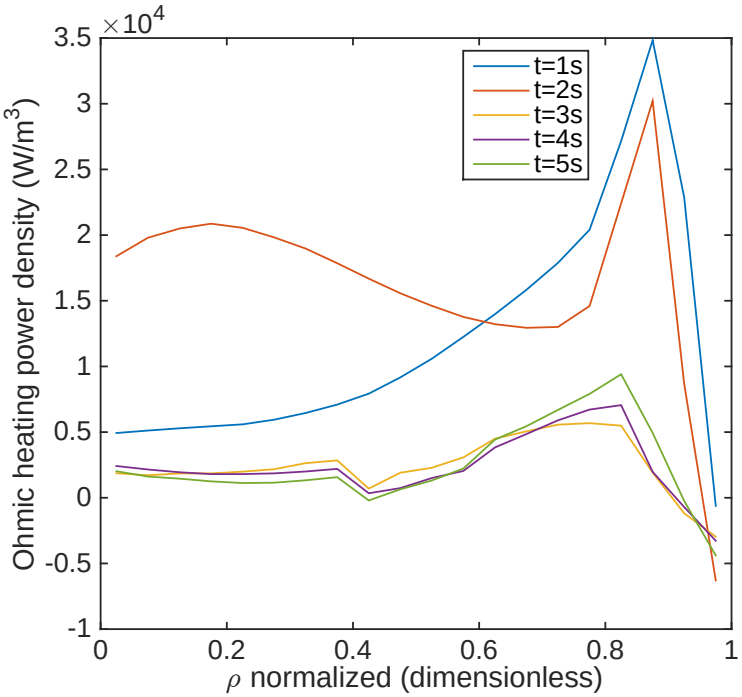

Figure 2.7: Ohmic heating density profiles for shot 147634.

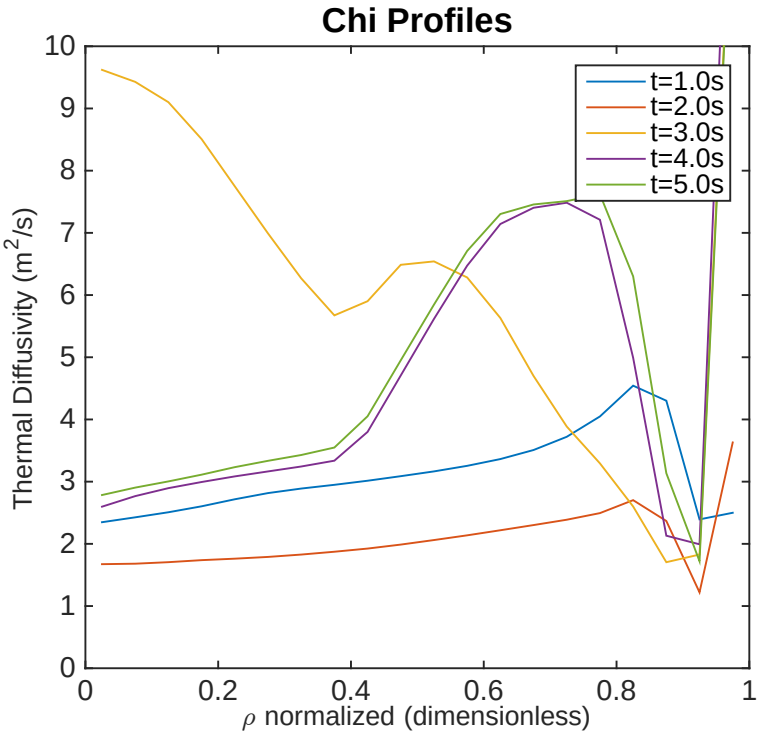

Figure 2.8: Thermal diffusivity profiles for shot 147634.

2.7 Comparison between Simulated Electron Temperatures and TRANSP profiles

With the geometric factors $(\hat{F}, \hat{G}, \hat{H})$, the density (n_e), heating inputs (Q_e), and thermal diffusivity (χ_e) all properly defined, the custom finite difference simulation was performed to model the electron temperature evolution for all times throughout the shot. Figures 2.9 and 2.10 display the results of this predictive simulation at a few key times.

In comparing the simulated profiles, the profile shape is paramount. As shown in Figure 2.10, the magnitude of the electron temperatures predicted by the EHTE solver appears to be lower than those predicted by TRANSP. However both the shape and the trend are consistent, in particular the exhibition of the H-mode pedestal. From the figure it is also clear that the profiles satisfy the boundary conditions, which state that the peak of the temperature is located at the center of the plasma $\hat{\rho} = 0$, and that the temperature drops to near zero at the boundary wall $\hat{\rho} = 1$. Clearly the simplified EHTE model proposed in this work is missing some physics that TRANSP is effective at capturing. Since the magnitude gap is consistent across the entire spatial domain, it is likely that additional heat that we have not modeled are causing the deviation and could be included in future developmental efforts of this model.

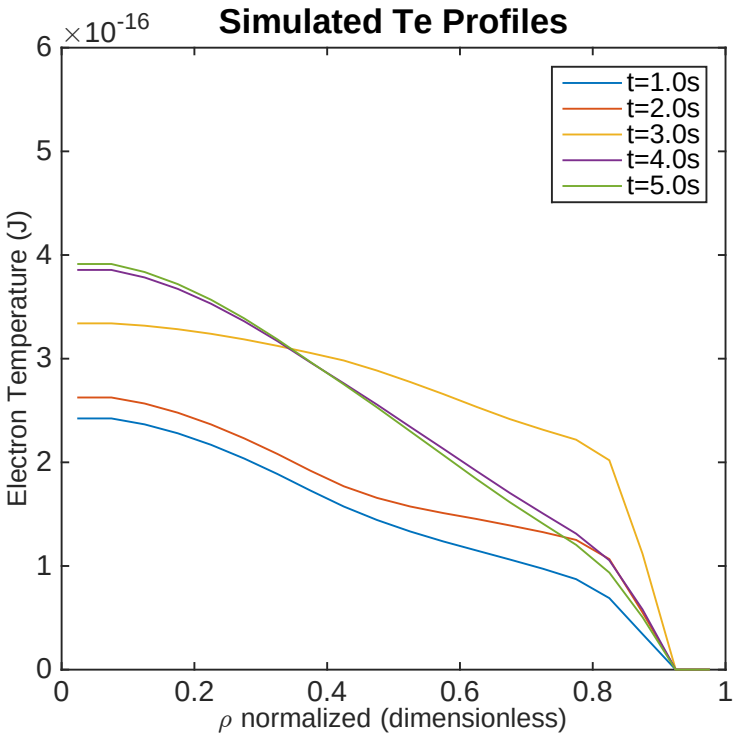

(a) Simulation-predicted T_e Profiles

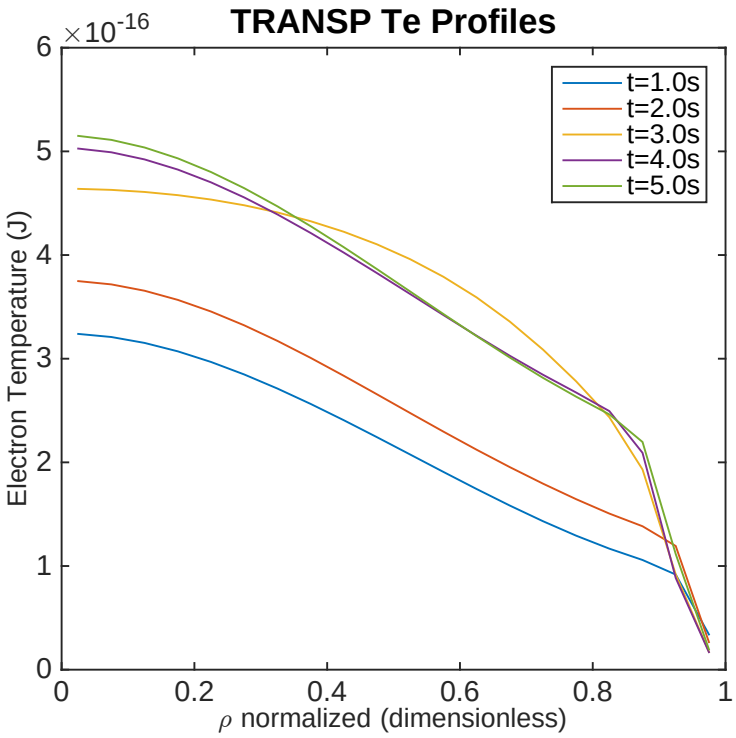

(b) TRANSP-predicted T_e Profiles

Figure 2.9: Electron temperature profiles predicted by (a) the custom hybrid finite difference solver of the EHTE and (b) the corresponding TRANSP simulations.

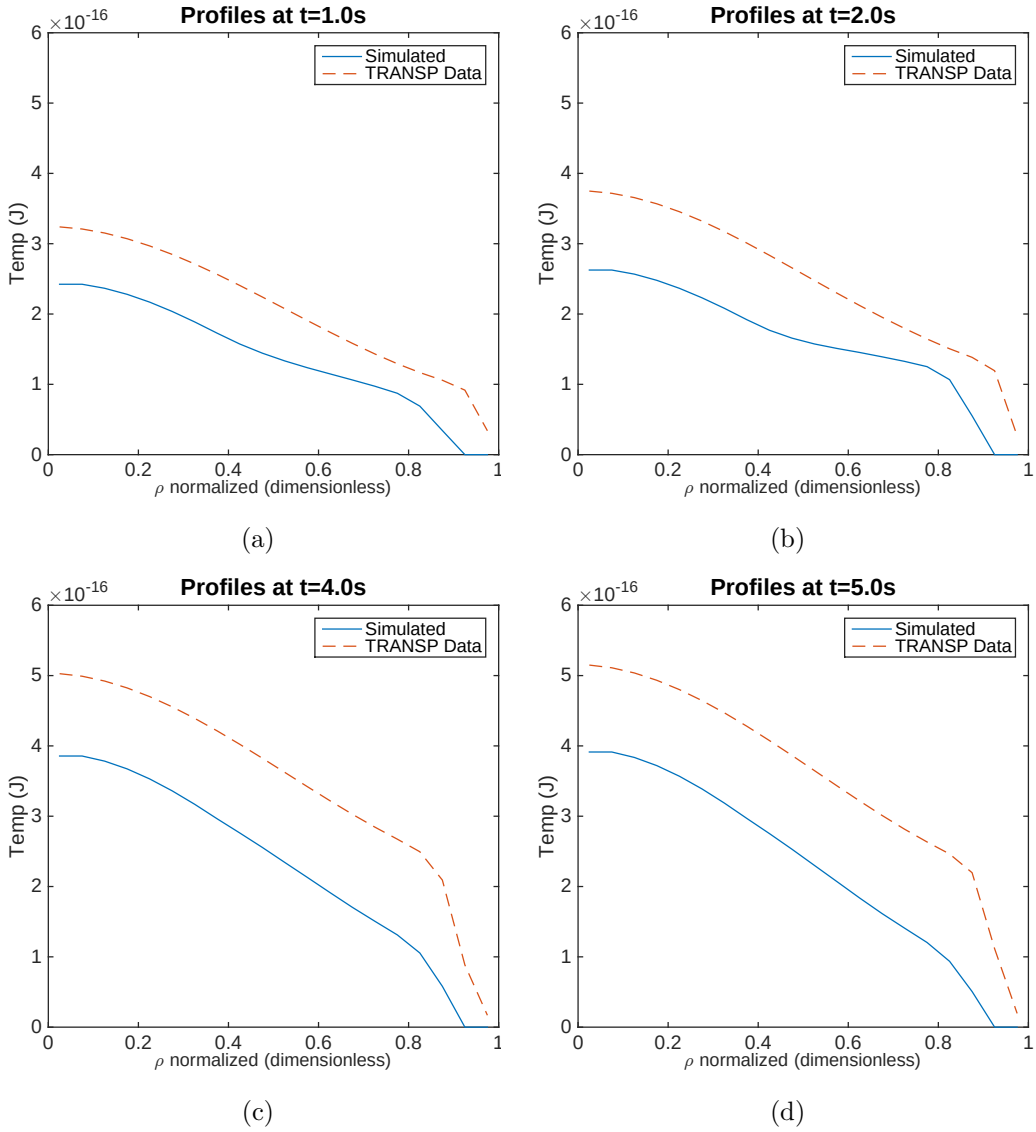

Figure 2.10: Electron temperature profiles predicted by the proposed EHTE solver and TRANSP at (a) 1 second, (b) 2 seconds, (c) 3 seconds, and (d) 4 seconds.

Chapter 3

Optimizing χ_e Through Spatial Interpolation

3.1 Modeling and Estimation of χ_e

The thermal conductivity (also called thermal diffusivity) of the electrons (χ_e) is a plasma parameter that plays a critical role in the EHTE since it indicates how the electron temperature diffusion varies across the minor effective radius of the tokamak. Since the plasma thermal diffusivity cannot be measured via traditional instrumentation, a model is necessary to be able to predict the evolution of the electron temperature. While complex physics-based model have been proposed for χ_e, there is a lack of a simple mathematical model for the thermal diffusivity that could be used for control design.

Previous work in this area includes the estimation of the plasma transport parameters using filtering theory. In [13], a general control-oriented transport model was proposed for plasma dynamics prediction and a stochastic filtering approach was developed based on an extended Kalman filter approach to provide real-time estimates of the poorly known or totally unknown transport coefficients. The work focused on time-constant to-be-estimated transport coefficients.

In this chapter, a different approach is followed by implementing a sequential quadratic programming (SQP) optimization method in order to estimate the thermal diffusivity profile. The to-be-optimized thermal diffusivity profile is modeled as a time-independent spatial profile reconstructed from values at seven spatial locations via interpolation. The free parameters of the optimization algorithm are the seven values from which the whole thermal diffusivity profile is reconstructed.

3.2 Basics to Sequential Quadratic Programming

When approaching nonlinearly constrained optimization problems, SQP is one of the most efficient approaches for converging to an accurate solution. This technique is frequently implemented in software packages like Matlab and Mathcad. SQP works off a Newtonian type optimization by calculating individual steps in response to perturbations and minimizing corresponding deviations.

The primary characteristic of SQP (and what gives SQP its name) is the replacement of the objective function with a quadratic approximation. For example let us consider the following nonlinear programming problem [14]:

$$\begin{aligned} \text{minimize} \quad & f(x) \\ \text{subject to} \quad & h(x) = 0 \\ & g(x) \leq 0 \end{aligned} \tag{3.1}$$

where $h(x)$ and $g(x)$ are the constraint functions, and $f(x)$ is the cost function to be minimized. The basic idea of sequential quadratic programming is to model a nonlinear programming problem at a given approximate solution, say x^k, by a quadratic programming subproblem, and then to use the solution to this subproblem to construct a better approximation x^{k+1} [14]. With enough iterations, convergence is achieved and $f(x)$ is successfully minimized. This minimization method is extrapolated from the quasi-Newtonian method for constrained optimization. As with the Newtonian solution and most iterative processes, initial

conditions that are located near the desired solution converge more rapidly than distant initial conditions.

When discussing Sequential Quadratic Programming, there are two classifications of convergence that heavily impact computational solving. "Local convergence" assumes that the given initial conditions fall close to the solution x^*. Using the proof of convergence of the classical Newton's method, the conditions generated for governing a local convergence ensure that the first order system of equations for iterations remain close to the solution, denoting that the quadratic subproblem is a good model for the nonlinear programming problem. If the starting position for the problem is distant from the solution, the convergence is called "global convergence". The main differentiator between local and global convergence is the introduction of a correct gradient and search direction, or merit function notated as ψ (this ψ is in no way related to the nuclear fusion term ψ, which represents magnetic flux). With the merit function describing descent as the primary indicator of convergence, iterations are assured to closer align themselves with the solution but do not force other local conditions such as the Hessian approximation [14]. Typically this means that local convergence is computationally simple and preferred over global convergence.

Let us examine the scalar valued Lagrangian function for the optimization problem (3.1), i.e.

$$\mathcal{L}(x, u, v) = f(x) + u^t h(x) + v^t g(x) \tag{3.2}$$

where u and v are the multiplier vectors and x is the vector for the gradient of the scalar-valued function $\nabla f(x)$. The vectors are all assumed to be column vectors and the "t" superscript is used to denote the transpose. In the basic SQP method, an approximation for x is chosen to be x^k. At the approximation x^k, the quadratic subproblem will have the form

$$(r^k)^t d_x + \frac{1}{2} d_x^t B_x d_x \tag{3.3}$$

subject to

$$\begin{aligned} \nabla h(x^k)^t d_x + h(x^k) &= 0 \\ \nabla g(x^k)^t d_x + g(x^k) &\leq 0 \end{aligned} \tag{3.4}$$

where r^k is taken to be the gradient of f at x^k, and B_k is the Hessian of the function. In (3.3) and (3.4), $d_x = x - x^k$, where the SQP method is focused on minimizing d_x.

Given the initial approximations x^0, u^0, v^0 and the merit function ψ, and setting k = 0, the basic algorithm for sequential quadratic programming is shown [14]:

1. Form and solve quadratic subproblem to obtain (d_x, d_u, d_v)
2. Choose steplength α so that $\psi(x^k + \alpha d_x) < \psi(x^k)$
3. Set $x^{k+1} = x^k + \alpha d_x$ $u^{k+1} = u^k + \alpha d_u$ $v^{k+1} = v^k + \alpha d_v$
4. Stop if converged
5. Compute B_{k+1}
6. Set $k := k + 1$; go to 1

(3.5)

As an example, a visualization of the SQP process for the nonlinearly constrained Rosenbrock's function is shown in Figure 3.1 [15]. Figure 3.1's display of the gradient lines shows how the descent direction of the convergence is applied giving the corresponding remote starting location and constraint boundary.

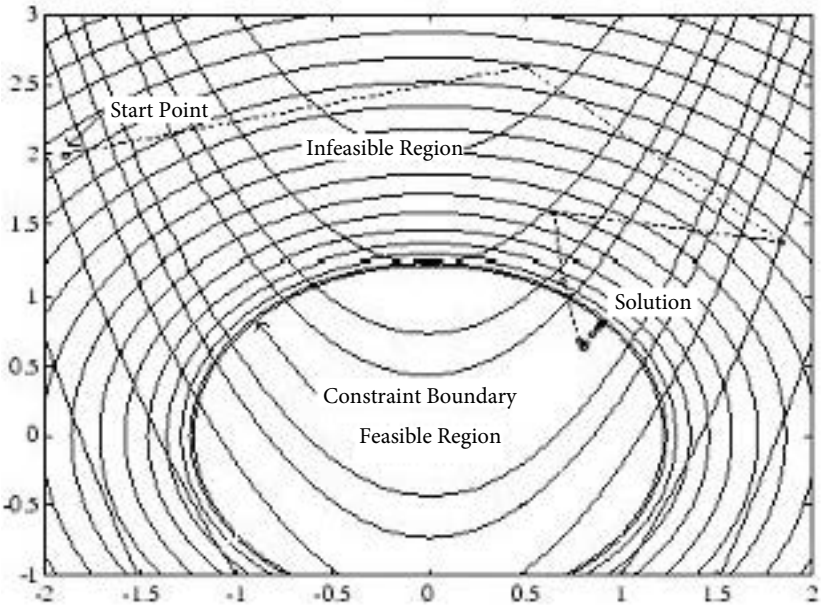

Figure 3.1: Plot detailing the SQP solving method for Rosenbrock's function, as supplied by Mathworks.

3.3 Predictive Model Used in Optimization

The EHTE numerical solver developed in previous chapters plays a key role in the optimization work presented in this chapter. First, the EHTE solver is used to generate the target profiles entering the to-be-minimized cost function. Second, the EHTE solver is used by the optimization algorithm to predict the evolution of the electron temperature profile for a given thermal diffusivity profile in each iteration of the optimization process.

For simulation purposes, a time span of 0.6-3.0 seconds has been used with a temporal step size of 0.02s, allocating a total of 121 temporal nodes. This allows us to test the accuracy of the solver without an unnecessary increase in computational time during the optimization process. Spatially, the minor axis was broken into 21 nodes, normalized by the variable $\hat{\rho}$ and setting $\hat{\rho} = 0$ to be the direct geometric center of the plasma and $\hat{\rho} = 1$ to be the edge of the plasma near the wall.

3.3.1 Geometric Factors

Previously in section 2.6, the geometric factors for shot 147634 were introduced. Since the magnitudes of these geometric factors deviate only slightly over time (under 10%), constant profiles for the geometric factors are assumed for the predictive model used for the estimation of the thermal diffusivity profile. Figure 3.2 exhibits the shape of these profiles.

3.3.2 Heating Sources

Whereas in the previous chapter the individual time-varying profiles for the heat deposition were shown, figures 3.3 and 3.4 consists of the combined heat sources active during the 121 temporal nodes relevant to this simulation. Both 3D and 2D visualizations are depicted. Analyzing Figure 3.4, one can note that this is the exact same total heating profile ($Q_e = Q_{ECE} + Q_{NBIs} + Q_{ohmic}$) presented in Section 2.6. However, the time length of the span has been cut to only the relevant temporal domain (0s - 3.0s). Prior to turning on the electrocycloton heating, only the ohmic heating (as a result of the plasma induced current) and the NBI heating contribute to the rise in temperature of the electrons. Thus it is expected that the simulation results will show a significant rise in T_e after temporal node 75 (2.1s).

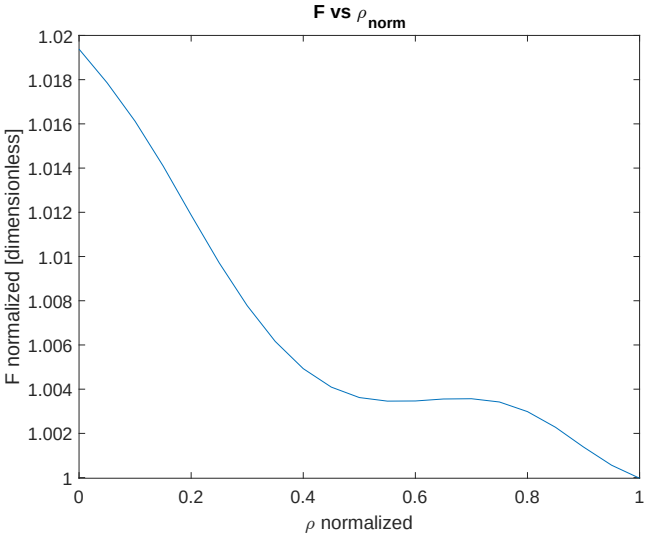

(a)

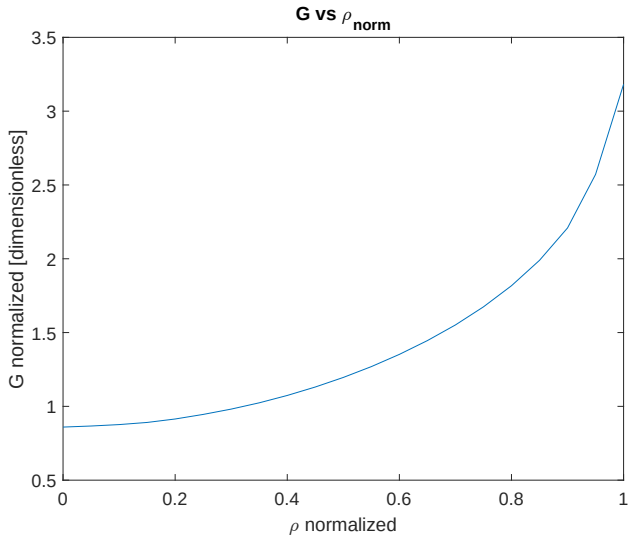

(b)

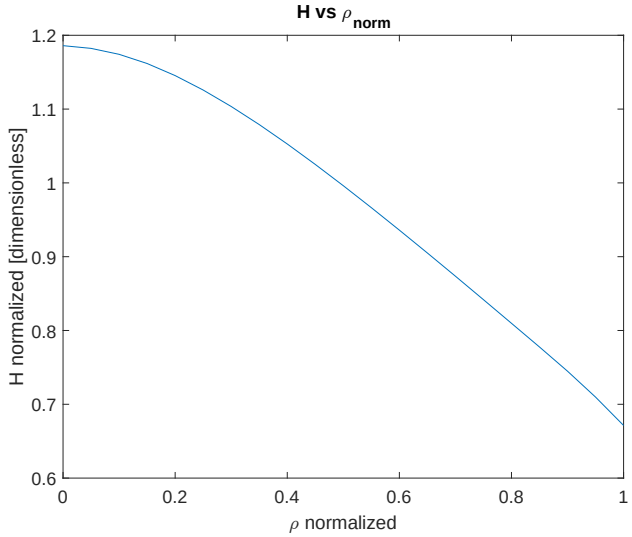

(c)

Figure 3.2: Time-averaged $F(\hat{\rho}), G(\hat{\rho}), H(\hat{\rho})$ profiles for χ_e optimization. Geometric factors extracted from TRANSP for DIII-D shot 147634.

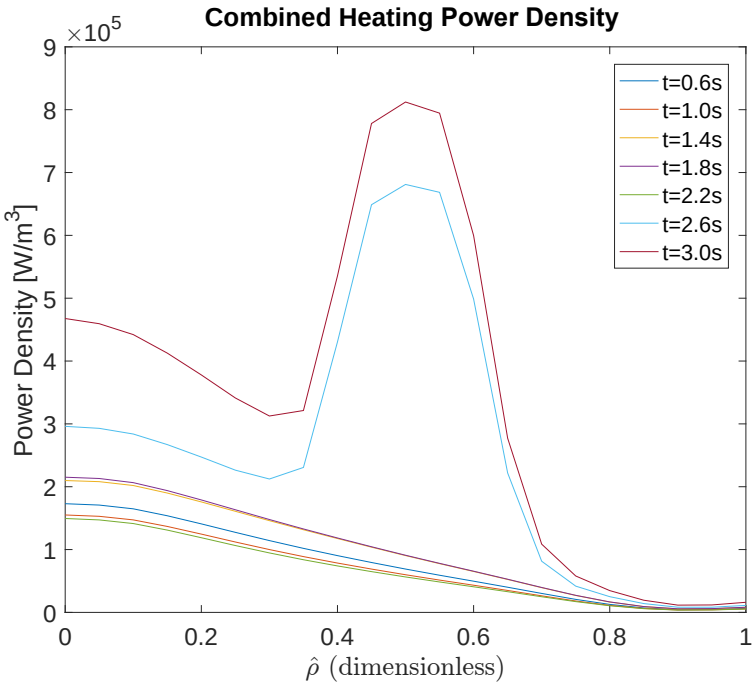

Figure 3.3: 2D Sample times of total combined heating energy during temporal span.

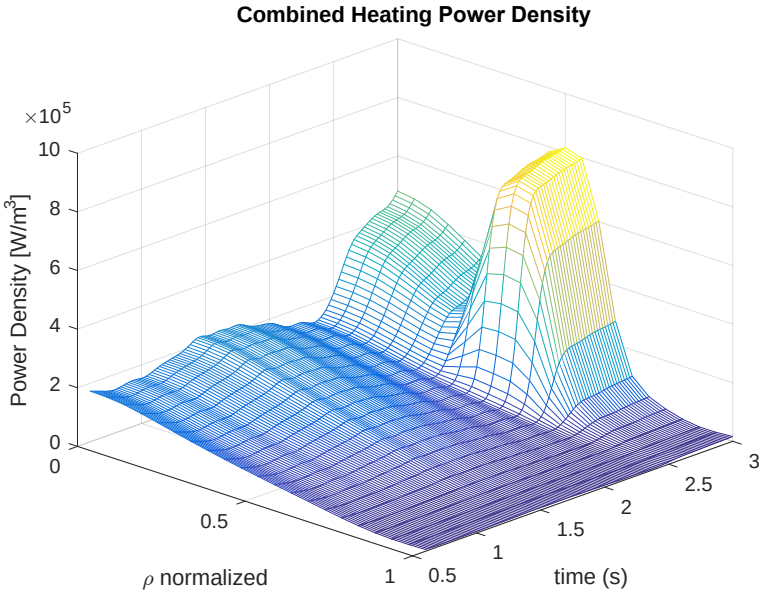

Figure 3.4: 3D Meshed plot of total combined heating energy over temporal span.

3.3.3 Electron Density

Unlike in Chapter 2, the electron density to be used in the EHTE during the optimization was not extracted from TRANSP, but modeled as

$$n_e(\hat{\rho}, t) = n_e^{prof}(\hat{\rho}) u_n(t) \tag{3.6}$$

where $n_e^{prof}(\hat{\rho})$ is a reference profile and $u_n(t)$ regulates the time evolution of the electron density. Note that n_e^{prof} is obtained by evaluating the experimental or simulated n_e at a reference time $t_{r_{ne}}$, i.e., $n_e^{prof}(\hat{\rho}) = n_e(\hat{\rho}, t_{r_{ne}})$ [16]. The electron density profile is modeled as such in Figure 3.5.

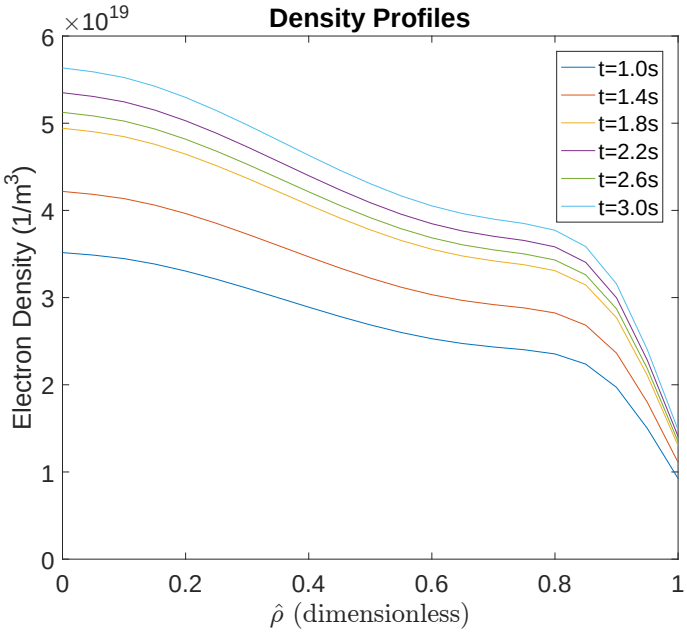

Figure 3.5: Modeled electron density profiles at select times.

3.3.4 Generation of Electron Temperature Target Profile

The goal of the SQP optimization algorithm developed in this chapter is to optimize the thermal diffusivity χ_e in the proposed EHTE model so that the predicted electron temperature matches a predefined target profile as closely as possible. While in practice the target profile will be obtained from experimental measure-

ments, in this work such profile is generated by simulations. Such simulations use a time-averaged diffusivity profile denoted as χ_e^{target} and shown in Figure 3.6. This profile was obtained by averaging over the time the χ_e evolution in shot 147634. With the indicated assumptions for the geometric factors, heating sources, electron density and thermal diffusivity, the EHTE-predicted evolution of the electron temperature profile, denoted as T_e^{target} hereafter, is displayed in Figure 3.7.

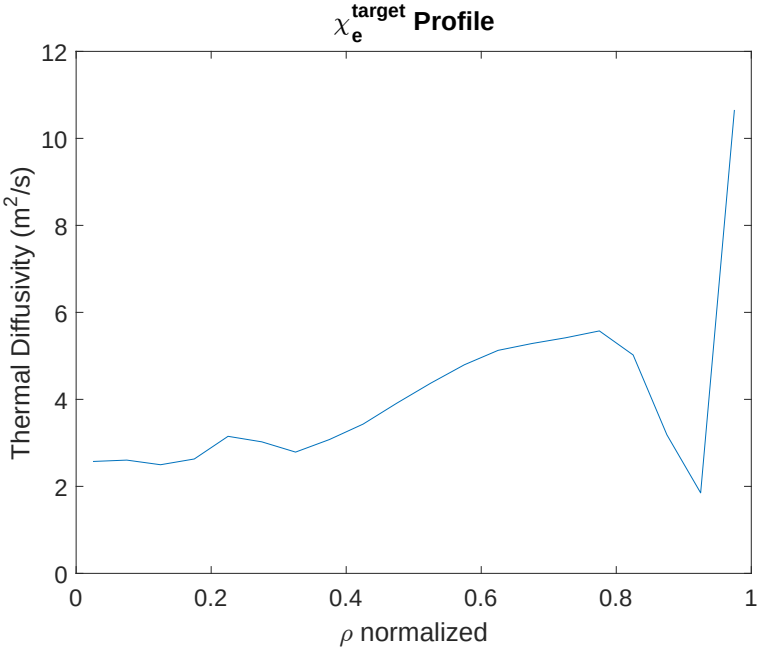

Figure 3.6: Time-averaged thermal diffusivity profile from TRANSP - used to predict T_e^{target}.

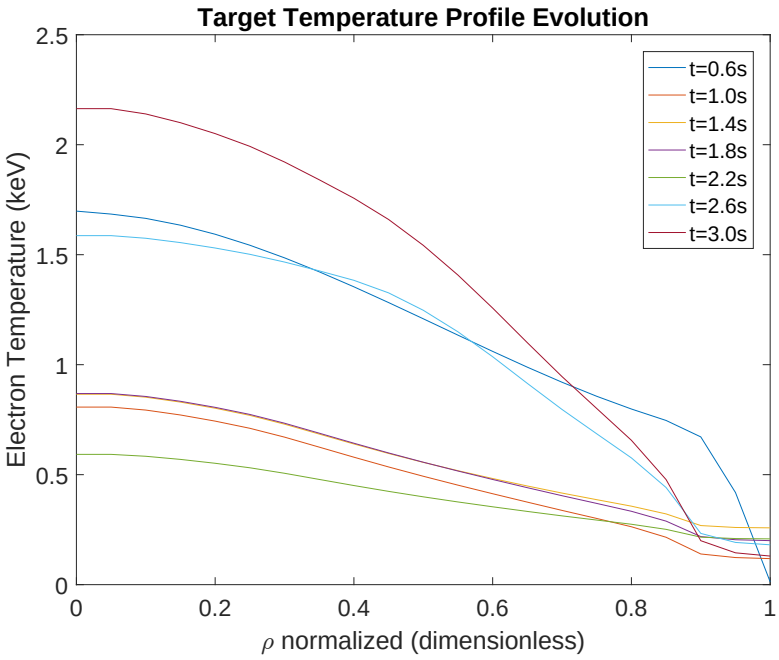

(a)

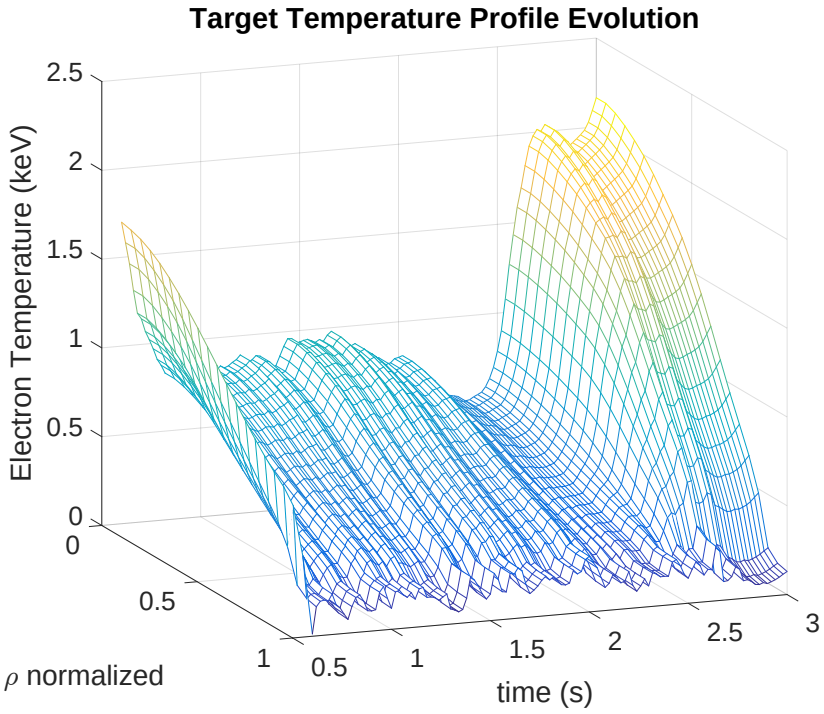

(b)

Figure 3.7: Target electron temperature profile predicted from the EHTE solution using TRANSP's time-averaged χ_e, in the form of (a) 2D plot at select times, and (b) 3D mesh of entire temporal domain.

3.4 Optimization Problem Definition

Now that T_e^{target} has been defined as the electron temperature profile predicted by the EHTE by using a time-averaged thermal diffusivity (χ_e^{target}), the optimization problem can be formally defined. The to-be-minimized cost function J is defined as

$$J = \int_0^{t_{final}} \int_0^1 \left(T_e^{target}(\hat{\rho}, t) - T_e^{opt}(\hat{\rho}, t)\right)^2 d\hat{\rho}dt. \tag{3.7}$$

The goal of the optimization algorithm is to modify (optimize) the initial guess for the thermal diffusivity profile, denoted $\chi_e^{initial}$, so that the electron-temperature-profile prediction by the EHTE, denoted as T_e^{opt}, based on the modified (optimized) thermal diffusivity profile, denoted as χ_e^{opt}, matches T_e^{target} as closely as possible. In this way, the cost function J is minimized.

The thermal diffusivity profile is modeled as a time-independent spatial profile reconstructed from values at seven spatial locations via interpolation. This parameterization of the to-be-optimized thermal diffusivity profile is necessary to carry out the optimization, since it models an infinite-dimensional profile by a finite number of to-be-optimized parameters. The free parameters of the optimization algorithm are therefore the seven values from which the whole thermal diffusivity profile is reconstructed. Thus, χ_e^{target} is indeed an approximated version of TRANSP's time-averaged diffusivity profile, as seen in Figure 3.8. The seven spatial nodes are carefully chosen to capture the shape of the typical thermal diffusivity profile in the most efficient possible manner. A series of spatial nodes evenly spaced across $\hat{\rho}$ may increase the difficulty of the optimizer to determine which node changes have the largest impact. Therefore, χ_e^{target} was segmented according to the following nodes and locations:

$$\begin{aligned} \chi_e^{target} &= [2.557, 2.564, 3.087, 2.932, 5.495, 2.518, 15.06] \\ \hat{\rho}_{crit}^{target} &= [0, 0.15, 0.25, 0.35, 0.8, 0.9, 1.0] \end{aligned} \tag{3.8}$$

where $\hat{\rho}_{crit}^{target}$ is defined as the critical locations along $\hat{\rho}$ that the corresponding

χ_e^{target} points are located. The target diffusivity nodes are interpolated in Figure 3.8(b). The $\chi_e^{initial}$ and χ_e^{opt} profiles are also prescribed as a nodal approximation.

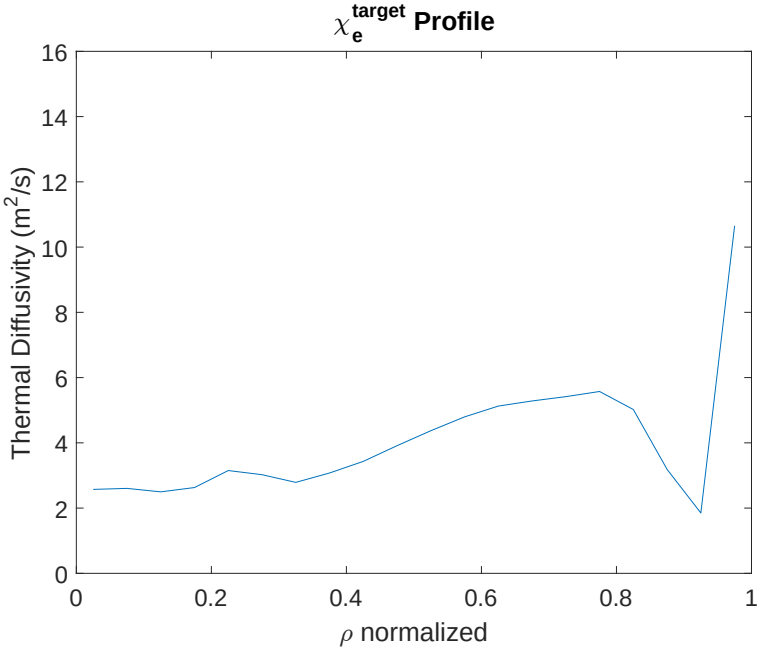

(a)

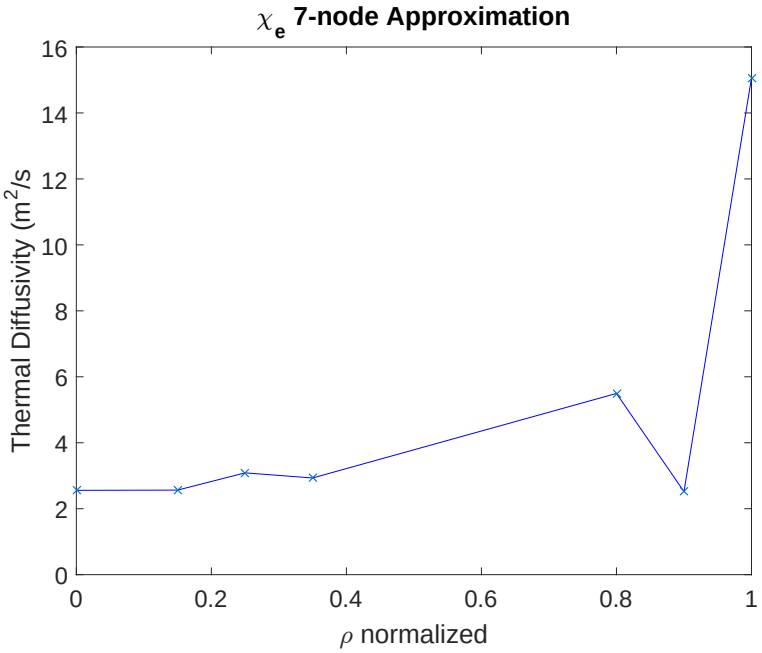

(b)

Figure 3.8: (a) time-averaged TRANSP 21-node χ_e^{target} profile and (b) 7-node χ_e^{target} approximation.

3.5 Testing Optimization Algorithm Against Varying Initial Conditions

Test 1 ($\chi_e^{initial} = 1.4\chi_e^{target}$): As the first test, the initial guess for the thermal diffusivity profile ($\chi_e^{initial}$) is established as exactly 140% of the target profile, at the same locations across the minor axis. The resulting array is described as

$$\begin{aligned} \chi_e^{initial} &= 1.4 * [2.557, 2.564, 3.087, 2.932, 5.495, 2.518, 15.06] \\ &= [3.580, 3.590, 4.322, 4.105, 6.293, 3.525, 21.084] \\ \hat{\rho}_{crit} &= [0, 0.15, 0.25, 0.35, 0.8, 0.9, 1.0] \end{aligned} \tag{3.9}$$

where the $\hat{\rho}_{crit}$ array listed in (3.9) describes the critical locations chosen. The converged solution to this profile optimizer can be seen in Figure 3.9. It is clear that the optimizer succeeded in pulling down the critical nodes to match the target diffusivity profile. The only distinct deviation from the target occurs within the first 3 nodes. This is likely due to the fact that the electron temperature profile is less sensitive to small variations of the value of the thermal diffusivity in the inner part of the plasma, which implies that they contribute less to the cost function.

To determine within what accuracy the solution achieved, we can calculate the error (δ) between $\chi_e^{optimized}$ and χ_e^{target} as

$$\begin{aligned} \chi_e^{target} &= [2.557, 2.564, 3.087, 2.932, 5.495, 2.518, 15.06] \\ \chi_e^{initial} &= [3.580, 3.590, 4.322, 4.105, 6.293, 3.525, 21.084] \\ \chi_e^{optimized} &= [2.9034, 2.8551, 2.6329, 3.1076, 5.5996, 2.4073, 14.556] \\ \delta_{nodal}^{\chi_e} &= [13.55\%, 11.35\%, -14.71\%, 5.99\%, 1.90\%, 4.40\%, 3.35\%] \end{aligned} \tag{3.10}$$

From (3.10) we can see that the optimization algorithm is successful in generating a profile that deviates only slightly from the target profile (on average less than 5%). However since the goal is to match electron temperature profiles, we can plot the target and the optimized profiles in Figure 3.10(a) and (b), respectively.

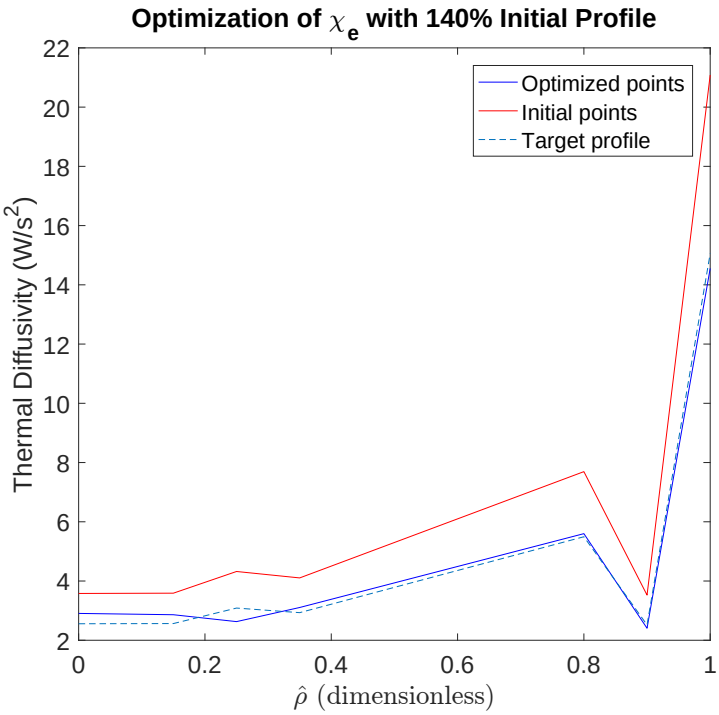

Figure 3.9: Compared $\chi_e^{optimized}$ and χ_e^{target} profiles, modeled with $\chi_e^{initial}$ as 140% of the χ_e^{target} profile.

It appears that using the optimized thermal diffusivity profile, the optimized electron temperature closely match the target temperature. This time we can calculate the difference between T_e^{opt} and T_e^{target} across all 21 spatial nodes. For simplicity, the compared values in (3.11) are from t=3.0 seconds.

$$\begin{aligned} T_e^{opt} - T_e^{target} = [&-0.0028, -0.0028, -0.0002, 0.0038, 0.0031, -0.0038, -0.0053, \\ &-0.0007, 0.0028, 0.0045, 0.0035, 0.0004, -0.0038, -0.0059, \\ &-0.0049, -0.0034, 0.0044, 0.0038, -0.0006, -0.0004, 0] \\ \delta_{nodal}^{T_e} = [&0.13\%, 0.13\%, 0.01\%, 0.12\%, 0.16\%, 0.20\%, 0.29\%, 0.04\%, \\ &0.16\%, 0.28\%, 0.24\%, 0.03\%, 0.31\%, 0.55\%, 0.54\%, 0.44\%, \\ &0.70\%, 0.84\%, 0.34\%, 0.30\%, 0.0\%] \end{aligned} \tag{3.11}$$

To have an average deviation from the target electron temperature profile of less than 1% is a very promising result. This implies that even though the first few nodes of the SQP optimized χ_e profile wandered from the target values, the prediction of electron temperatures was not affected by this discrepancy.

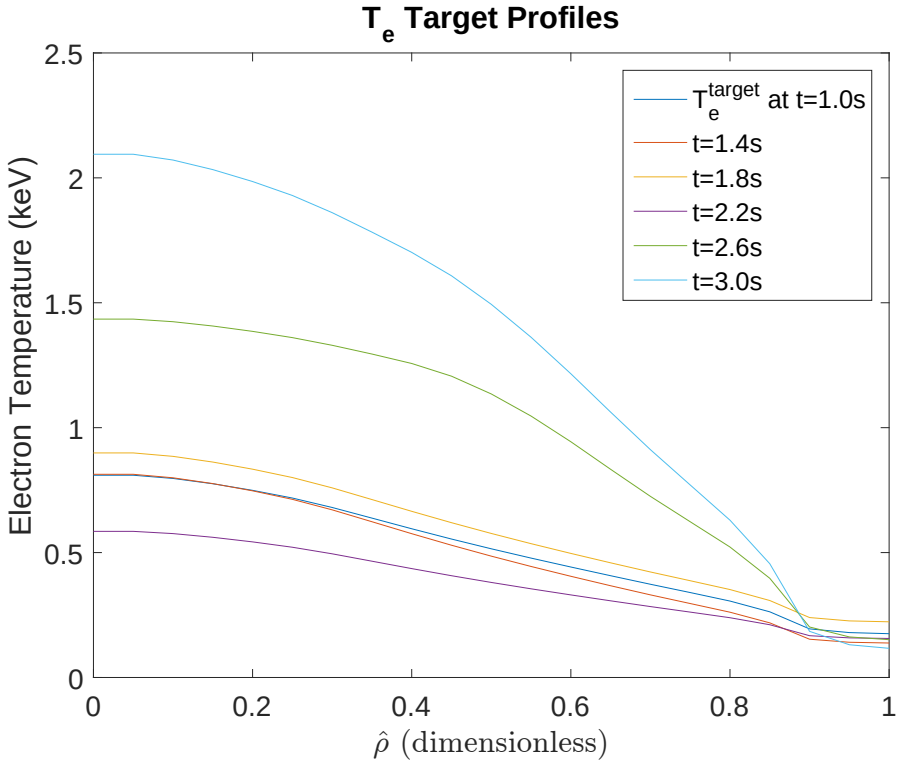

(a)

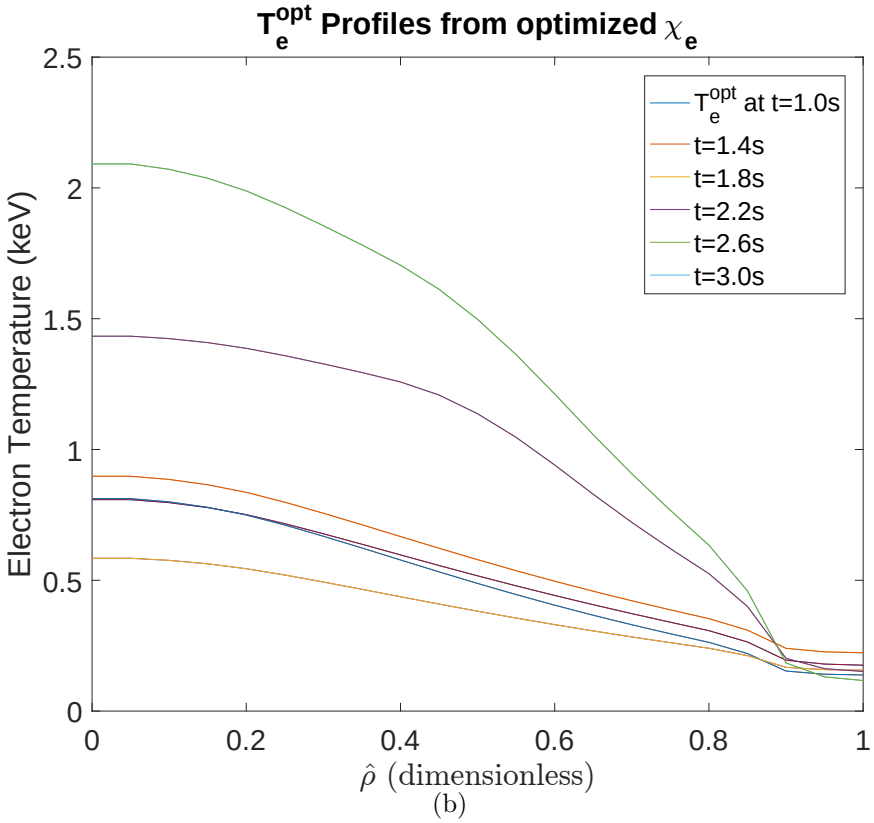

(b)

Figure 3.10: Comparison between (a) target electron temperature profiles and (b) optimized electron temperature profiles when $\chi_e^{initial} = 1.4\chi_e^{target}$.

Test 2 ($\chi_e^{initial} = 0.6\chi_e^{target}$): Now that the ability of the solver to converge to a target χ_e profile when prescribed a much higher initial profile has been proven, we can be confident that the SQP optimizer accepts negative gradients and search directions. The next test is to prescribe an initial profile that is beneath the target curve to monitor the effects of a positive gradient and search direction. Identifying the 60% initial conditions in a similar manner as (3.9):

$$\begin{aligned} \chi_e^{initial} &= 0.6 * [2.557, 2.564, 3.087, 2.932, 5.495, 2.518, 15.06] \\ &= [1.5342, 1.5384, 1.8522, 1.7592, 3.297, 1.5108, 9.036] \\ \hat{\rho}_{crit} &= [0, 0.15, 0.25, 0.35, 0.8, 0.9, 1.0] \end{aligned} \tag{3.12}$$

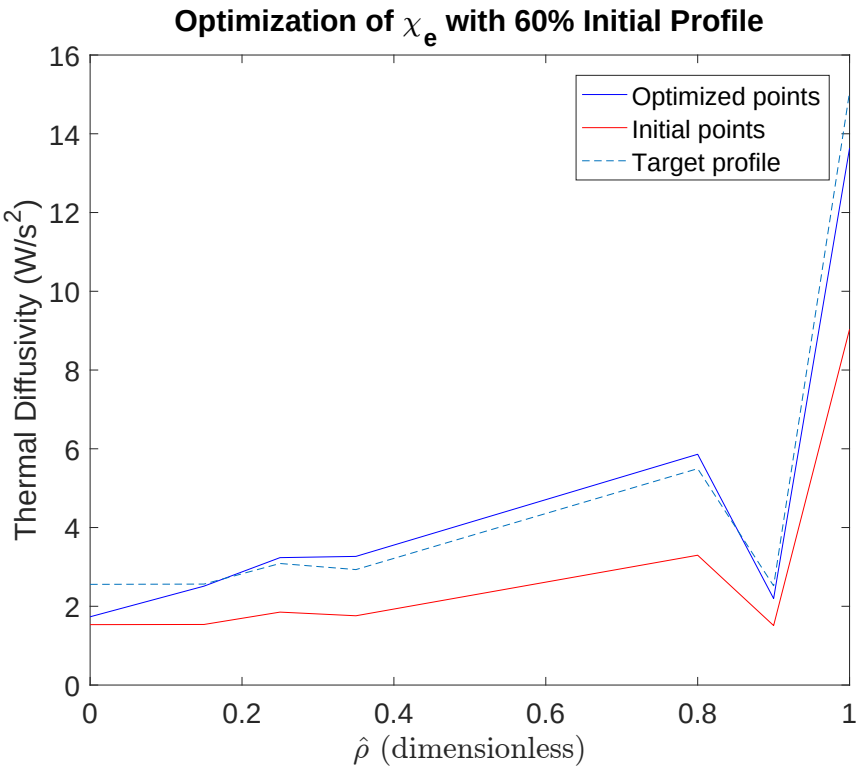

Figure 3.11: Compared χ_e^{opt} and χ_e^{target} profiles, modeled with $\chi_e^{initial}$ as 60% of the χ_e^{target} profile.

As shown in Figure 3.11, again the optimizer succeeds in closely matching all nodes after $\hat{\rho} = 0.25$, but wanders from the target in the inner nodes, especially at

the plasma center. From a strictly χ_e-matching perspective, the difference between the optimized profile and the target can be calculated as in (3.10). But since the cost function is concerned solely with the electron temperature matching, the more appropriate comparison is in regards to the T_e profiles. In Figure 3.12, the target temperature profile lines are shown with the optimized temperatures displayed as "x" markers. The comparison shows a very close match.

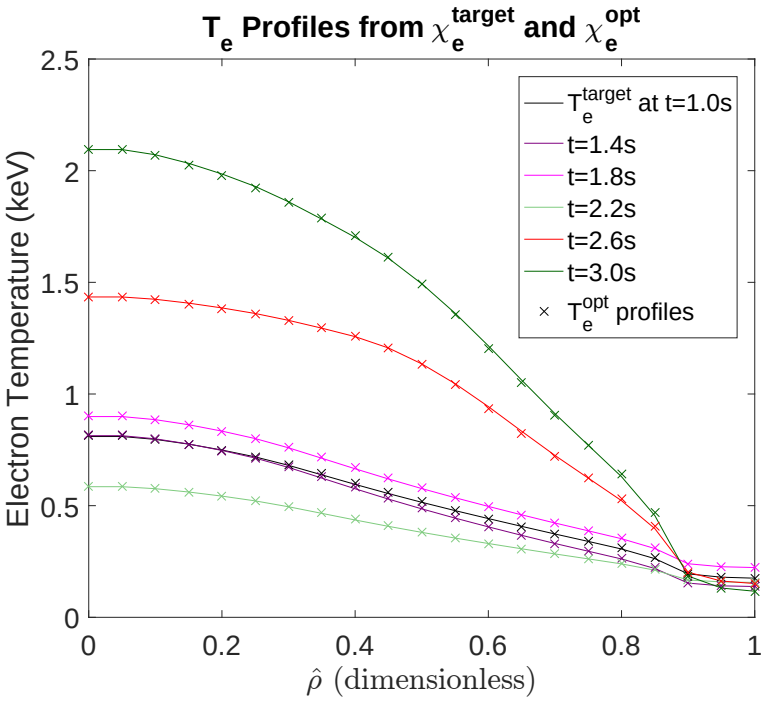

Figure 3.12: Comparison between target and optimized temperature profiles, with $\chi_e^{initial}$ as 60% of the χ_e^{target} profile.

From Figure 3.12 it is clear that the optimization algorithm has no issues solving the SQP quadratic subfunctions and converging on the target temperatures regardless of the fact that the initial condition for the thermal diffusivity is below the target profile. To the naked eye the optimized profile at the nodes seems to match the target perfectly. The deviation for this particular 60% initial condition

optimization is given by

$$\begin{aligned} T_e^{opt} - T_e^{target} = [&0.0011, 0.0011, -0.0042, -0.0074, -0.0084, -0.0073, -0.0019, \\ &0.0045, 0.0065, 0.0049, 0.0002, -0.0058, -0.0106, -0.0107, \\ &-0.0056, 0.0011, 0.0145, 0.0161, -0.0025, -0.0014, 0.0] \\ \delta_{nodal}^{T_e} = [&0.05\%, 0.05\%, 0.20\%, 0.36\%, 0.42\%, 0.38\%, 0.10\%, 0.25\%, \\ &0.38\%, 0.31\%, 0.01\%, 0.43\%, 0.87\%, 1.01\%, 0.62\%, 0.14\%, \\ &2.30\%, 3.53\%, 1.36\%, 1.09\%, 0.0\%] \end{aligned} \tag{3.13}$$

Comparing the error to the first test, it is evident that the optimization results are consistent between the two tests with separate $\chi_e^{initial}$ profiles. Before moving on to refine the optimization procedure, we must test the ability of the algorithm to minimize the electron-temperature matching error when the prescribed initial condition that does not hold the same general shape of χ_e^{target}.

Test 3 (Flat Line as Initial Condition): Tests 1 and 2 showed that, given a $\chi_e^{initial}$ profile resulting from multiplying the χ_e^{target} profile by constants both smaller and greater than one, an SQP algorithm can be implemented that predicts the electron temperatures from a hybrid finite difference method and computes the appropriate cost function, minimizing the error and converging to the target profile within a 1% error. But for both applications the input profile held the major shape of the target profile that was simply translated vertically on the graph. The final test for determining the capability of the optimization algorithm is to ascertain whether a completely random $\chi_e^{initial}$ profile, with a general shape that does not match the target profile, will still converge upon a $\chi_e^{optimized}$ that predicts matching electron temperatures to the target. To do this, the initial condition was described as a straight line, i.e.

$$\begin{aligned} \chi_e^{initial} &= [5.0, 5.0, 5.0, 5.0, 5.0, 5.0, 5.0] \\ \hat{\rho}_{crit} &= [0, 0.15, 0.25, 0.35, 0.8, 0.9, 1.0] \end{aligned} \tag{3.14}$$

With this initial condition case of a flat line $\chi_e^{initial}$ profile, the optimization model was for a third time successful in identifying a $\chi_e^{optimized}$ profile that resulted in closely matching electron temperatures. The optimized thermal diffusivity can be seen in Figure 3.13, with the corresponding temperature predictions in Figure 3.14. Note in Figure 3.13 the rapid drop and following increase of slope after $\hat{\rho} = 0.8$; this implies that the H-mode pedestal will be present in the electron temperature profiles, which is confirmed in Figure 3.14. For $\hat{\rho} \leq 0.2$, χ_e^{opt} shows once again a relatively large deviation from χ_e^{target}; however, as before, this has a small effect on the predicted electron temperature, since in Figure 3.14 it is clear that the matching is good. If T_e profile does not depend heavily on the inner values of the χ_e profile, the values can fluctuate around an average value while still producing the correct T_e profile.

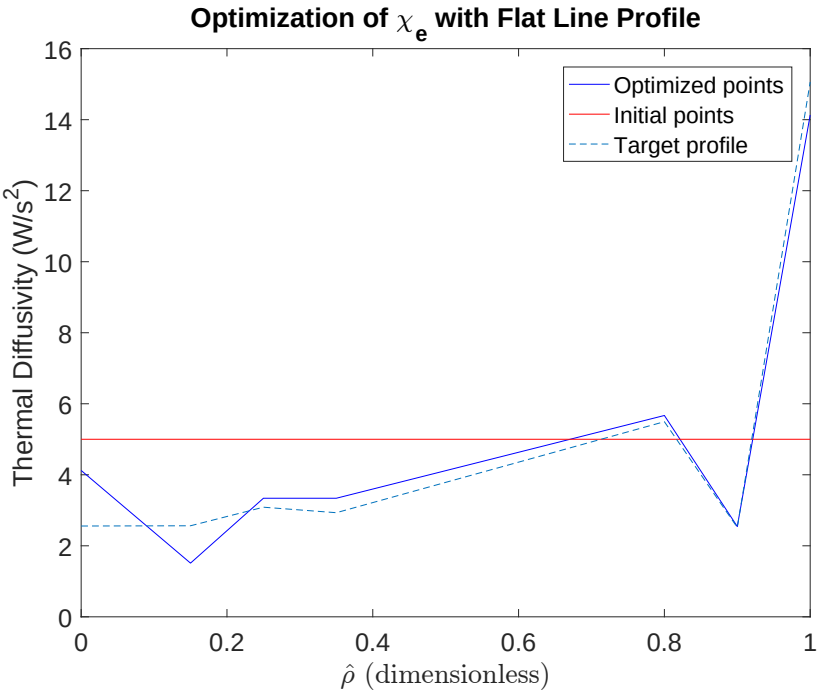

Figure 3.13: Compared $\chi_e^{optimized}$ and χ_e^{target} profiles, modeled with $\chi_e^{initial}$ as a flat line profile.

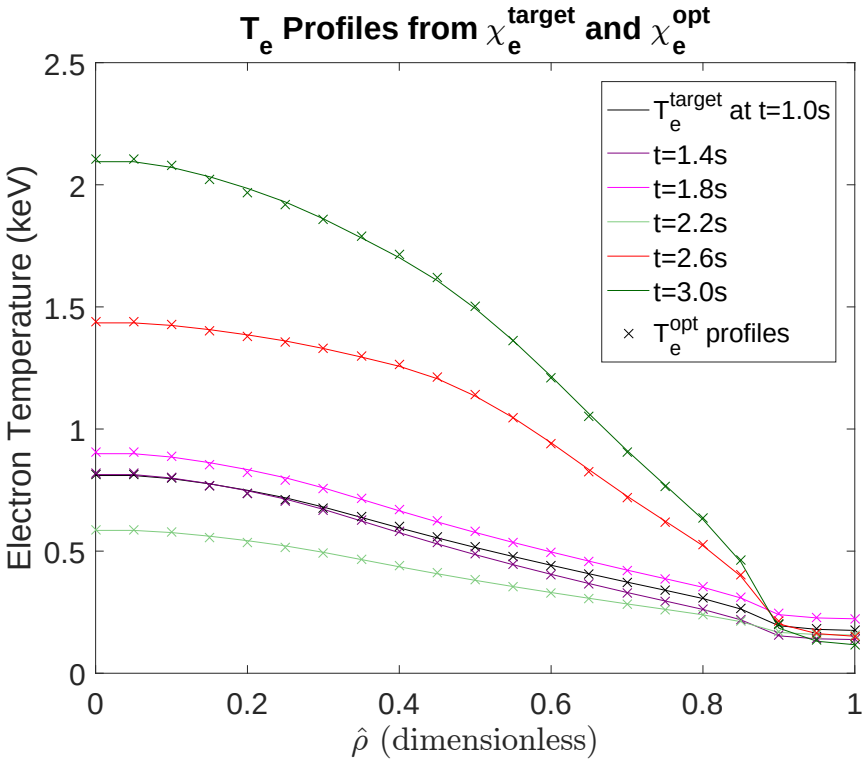

Figure 3.14: Compared target and optimized temperature profiles, with $\chi_e^{initial}$ as a flat line profile.

The deviation between T_e^{opt} and T_e^{target} is given by

$$\begin{aligned} T_e^{opt} - T_e^{target} = [&0.0130, 0.0130, 0.0087, -0.0092, -0.0140, -0.0070, 0.0029, \\ &0.0117, 0.0150, 0.0134, 0.0072, -0.0016, -0.0103, -0.0148, \\ &-0.0141, -0.0115, -0.0022, 0.0035, 0.0215, 0.0062, 0.0] \end{aligned} \tag{3.15}$$

with the nodal error percentages calculated to be

$$\begin{aligned} \delta_{nodal} = [&0.62\%, 0.62\%, 0.42\%, 0.45\%, 0.71\%, 0.36\%, 0.16\%, 0.66\%, 0.88\%, \\ &0.84\%, 0.48\%, 0.12\%, 0.85\%, 1.40\%, 1.55\%, 1.50\%, 0.34\%, 0.78\%, \\ &11.65\%, 4.71\%, 0.0\%] \end{aligned} \tag{3.16}$$

3.6 Conclusions

In this chapter, a Sequential Quadratic Programming (SQP) optimization algorithm was implemented with the goal of identifying the thermal diffusivity profile, which is part of the EHTE, so that the evolutions of the electron temperature profile closely match predefined target profile evolutions. The to-be-minimized cost function was defined as the spatial-temporal integral of the quadratic error between predicted (by the numerical EHTE solver) and target electron temperature profiles. The target electron temperature profile was generated by the EHTE solver by using a time-averaged thermal diffusivity profile and simplified models for the geometric factors, electron density and heating sources. The to-be-optimized thermal diffusivity profile was modeled as a time-independent spatial profile reconstructed from values at seven spatial locations via interpolation. The free parameters of the optimization algorithm were the seven values from which the whole thermal diffusivity profile was reconstructed. The optimization algorithm was effective in converging to a thermal diffusivity profile that predicted a temperature profile evolution closely matching the target profile.

Chapter 4

Optimizing χ_e Through Spatial Interpolation (Augmented Cost)

4.1 Incorporating the Magnetic Flux Into the Cost Function

In the previous chapter, the optimization algorithm converged to a χ_e profile based on a cost function that was solely dependent on the electron temperature profile. Recalling the magnetic diffusion equation previously described in Section 1.5, it is clear that the electron temperature profile has a large impact on the magnetic flux ψ, since the plasma resistivity is a function of the electron temperature. Therefore, we are interested in finding a χ_e profile that minimizes both the electron temperature and the magnetic flux matching errors. For this reason it is important to alter the cost function to include the deviation in magnetic flux from the target flux profile. To do this, the cost function (3.7) is modified as

$$J = \int_0^{t_{final}} \int_0^1 \left(T_e^{target}(\hat{\rho},t) - T_e^{opt}(\hat{\rho},t)\right)^2 + \left(\psi^{target}(\hat{\rho},t) - \psi^{opt}(\hat{\rho},t)\right)^2 d\hat{\rho}dt \tag{4.1}$$

The ψ^{target} profile is obtained in the same manner as T_e^{target}, i.e. the time-averaged thermal diffusivity profile computed by TRANSP for DIIII-D shot 147634, referred

to as χ_e^{target}, is inserted into the predictive model and the numerical solvers for both the EHTE and MDE are used to produce simulated targets. Figure 4.1 displays the poloidal magnetic flux target profiles generated by this method.

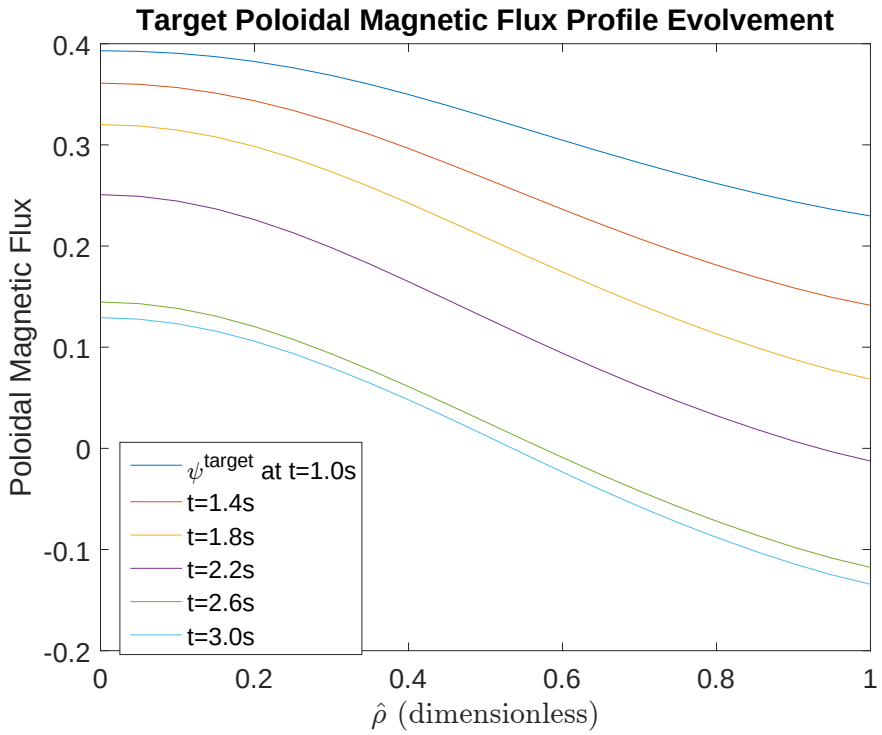

Figure 4.1: Target poloidal magnetic flux profiles at select times.

To examine how this affects the product of the optimization, the same three tests from the previous chapter are performed, but now with different results due to the introduction of the matching error for ψ in the cost function. For this chapter, some of the initial conditions are moved slightly to help distinguish these results from the previous chapter's.

4.2 Testing Optimization Algorithm Against Varying Initial Conditions

Test 1 ($\chi_e^{initial} = 1.5\chi_e^{target}$)**:** Using an initial value of the χ_e profile equal to $1.5\chi_e^{target}$, the optimization algorithm is successful in converging upon a profile that appears to more closely match the target χ_e profile, particularly in the inner nodes, due to the added constraints in the cost function in terms of the magnetic flux profile, as seen in Figure 4.2. With the introduction of the ψ matching error in the cost function, an increase of the electron-temperature-profile matching error may be expected because the algorithm looks for a thermal diffusivity that optimally solve the tradeoff between matching errors now present in the cost function.

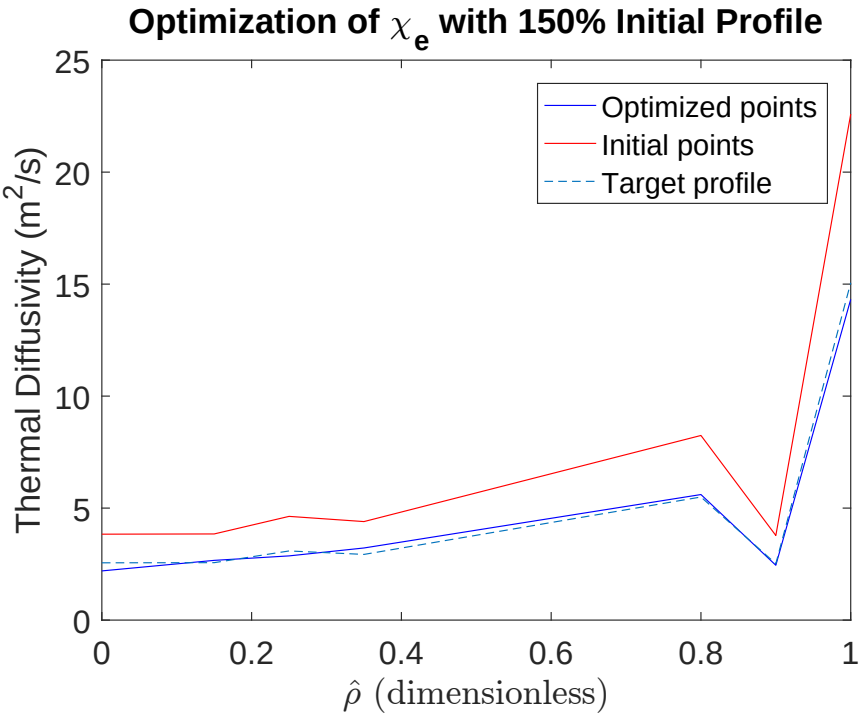

Figure 4.2: Comparison of χ_e^{opt} and χ_e^{target} profiles, modeled with $\chi_e^{initial}$ as 150% of the χ_e^{target} profile.

With the χ_e^{opt} attained for this test, we can compare the optimized electron-temperature and magnetic-flux profiles to their targets, as seen in Figure 4.3.

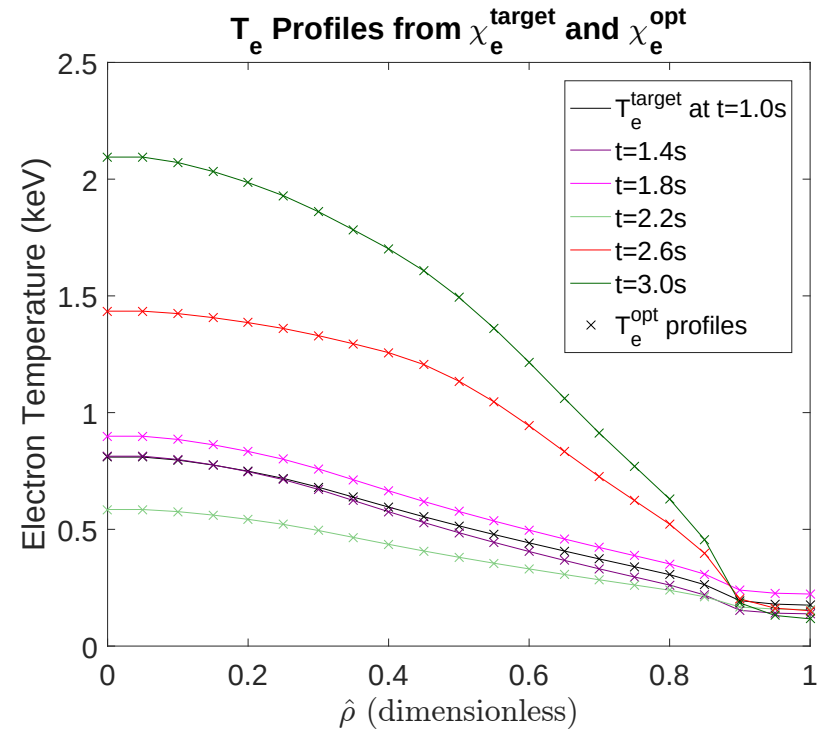

(a)

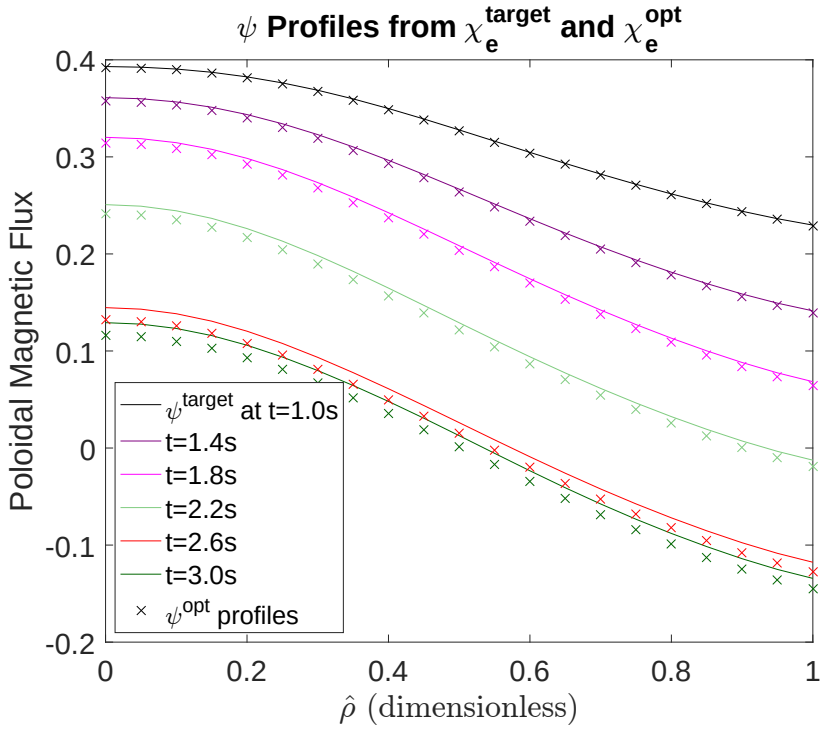

(b)

Figure 4.3: Compared target and simulated (a) temperature profiles and (b) magnetic flux profiles, with $\chi_e^{initial}$ as 150% of the χ_e^{target} profile.

Repeating the analysis process from the previous chapter, we can examine the resulting errors. For simplicity, only the average error is presented for the electron temperature and the magnetic flux.

$$\begin{aligned} \delta^{\chi_e}_{nodal} &= [13.84\%, 3.85\%, 7.09\%, 9.82\%, 2.03\%, 2.84\%, 4.96\%] \\ \delta^{\chi_e}_{ave} &= 6.35\% \qquad \delta^{T_e}_{ave} = 0.182\% \qquad \delta^{\psi}_{ave} = 2.06\% \end{aligned} \tag{4.2}$$

As before, $\delta^{\chi_e}_{nodal}$ is defined as the percent deviation between χ_e^{target} and χ_e^{opt} at each spatial node, while $\delta^{\chi_e}_{ave}$, $\delta^{T_e}_{ave}$, and δ^{ψ}_{ave} are the average error percentages over the spatial domain of the thermal diffusivity, electron temperature and magnetic flux.

Graphically, the nodal errors can be displayed in order to identify which area of the spatial domain carries the largest error. Figure 4.4 shows the deviation for a few specific times of the optimized temperature and flux profiles from their targets. From Figure 4.4, it is possible to note that even at peak error neither the electron temperature nor the magnetic flux diverge more than 5% from the target values. This is valid for all spatial locations and time within the simulation range. For the center of the plasma, the error between optimized and target temperatures and magnetic fluxes are very small. Larger deviations occur near the end of the spatial domain at the plasma boundary for the electron temperature, and halfway to the boundary (at $\hat{\rho} = 0.5$) for the magnetic flux. Comparing these observations with the optimized profiles in Figure 4.3, this error is hardly noticed.

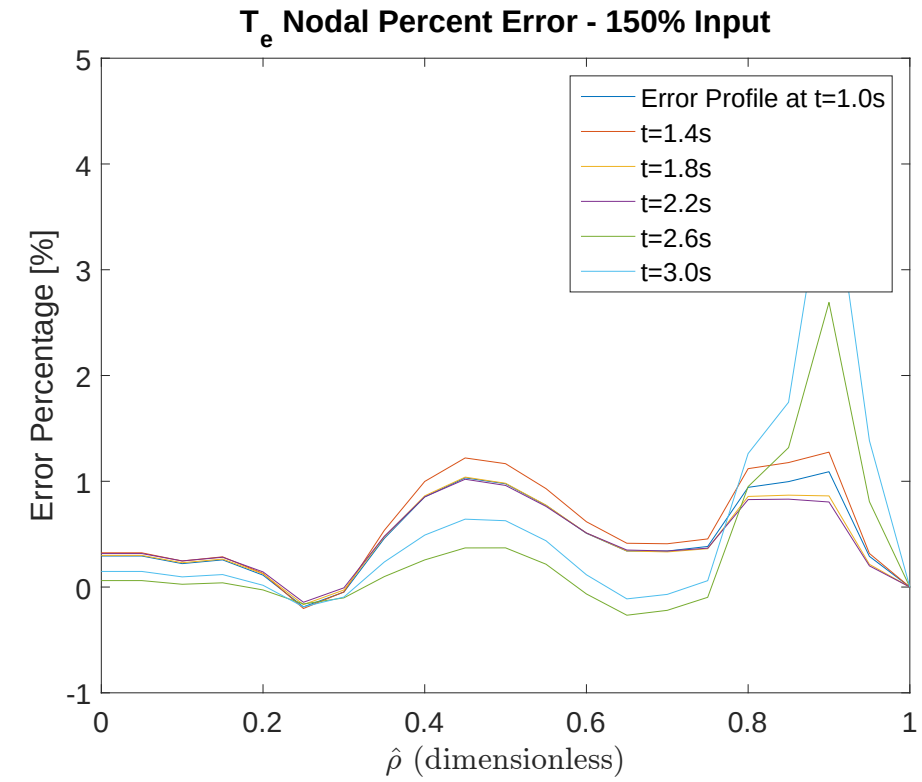

(a)

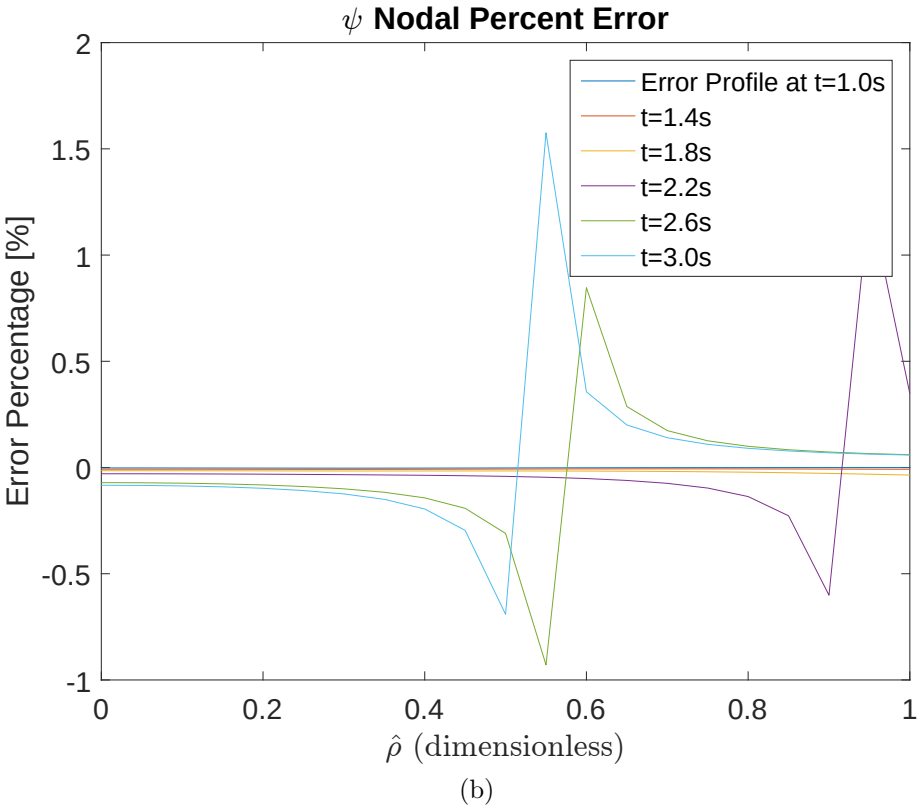

(b)

Figure 4.4: Error analysis for (a) T_e and (b) ψ, when $\chi_e^{initial} = 1.5 * \chi_e^{target}$.

Test 2 ($\chi_e^{initial} = 0.6\chi_e^{target}$)**:** As in the previous tests, the initial condition is prescribed at exactly 60% the magnitude of χ_e^{target}. The resulting output is shown in Figure 4.5, where χ_e^{opt} and χ_e^{target} are compared, and the average error percentages have been identified as

$$\begin{aligned} \delta_{ave}^{\chi_e} &= 11.61\% \\ \delta_{ave}^{T_e} &= 0.267\% \\ \delta_{ave}^{\psi} &= 2.17\% \end{aligned} \tag{4.3}$$

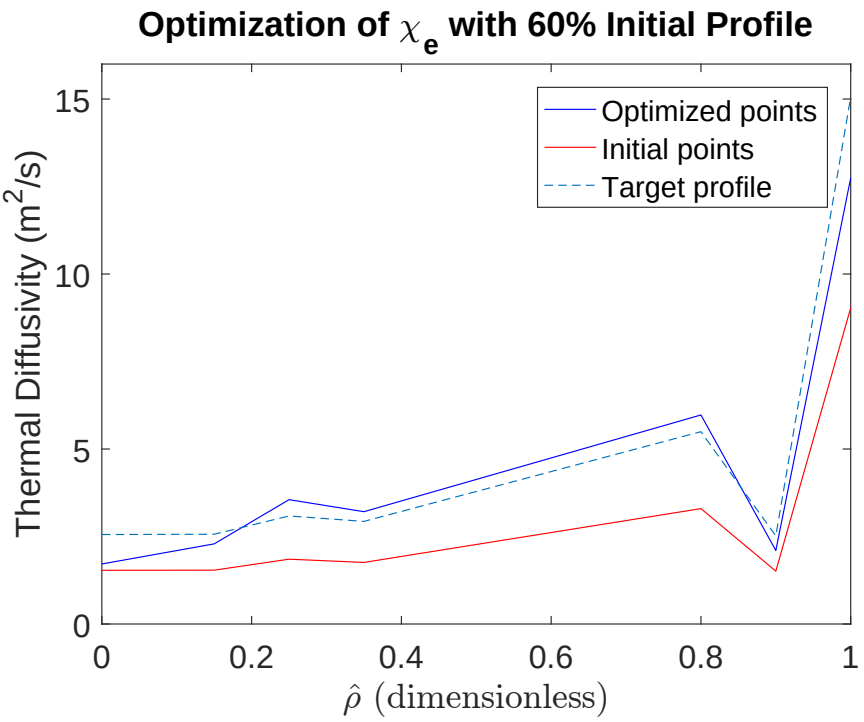

Figure 4.5: Comparison of χ_e^{opt} and χ_e^{target} profiles, modeled with $\chi_e^{initial}$ as 60% of the χ_e^{target} profile.

The resulting χ_e^{opt} is then used to predict both T_e^{opt} and ψ^{opt}, which are shown in Figure 4.6.

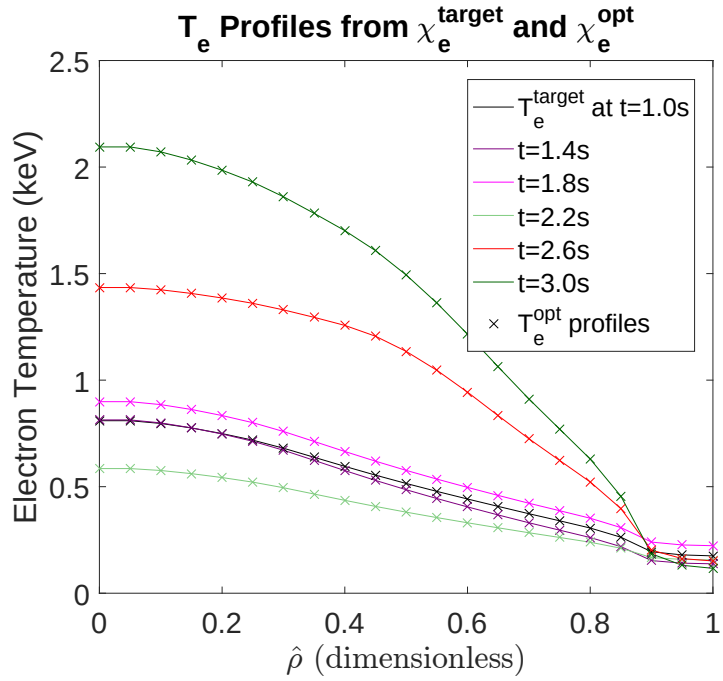

(a)

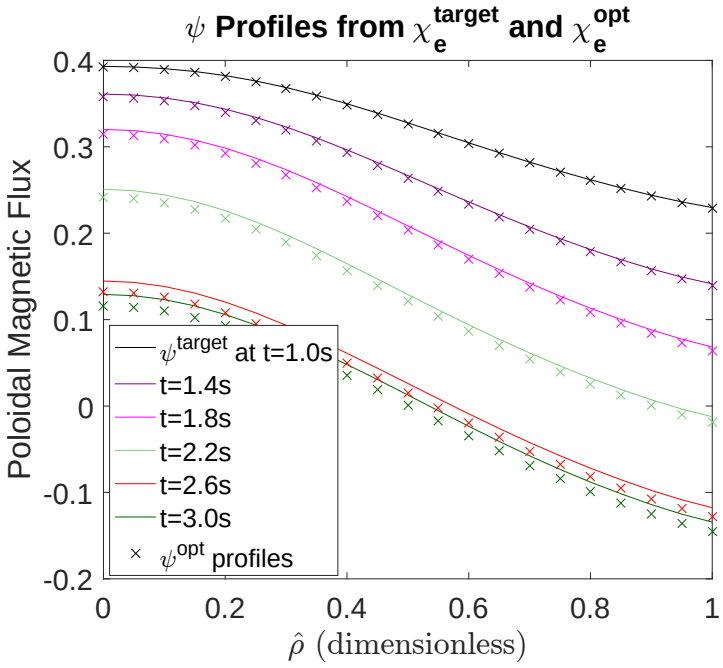

(b)

Figure 4.6: Compared target and simulated (a) temperature profiles and (b) magnetic flux profiles, with $\chi_e^{initial}$ as 60% of the χ_e^{target} profile.

As in Test 1, we can show the error changing along the spatial domain in Figure 4.7, which exhibits a pattern similar to that in Test 1.

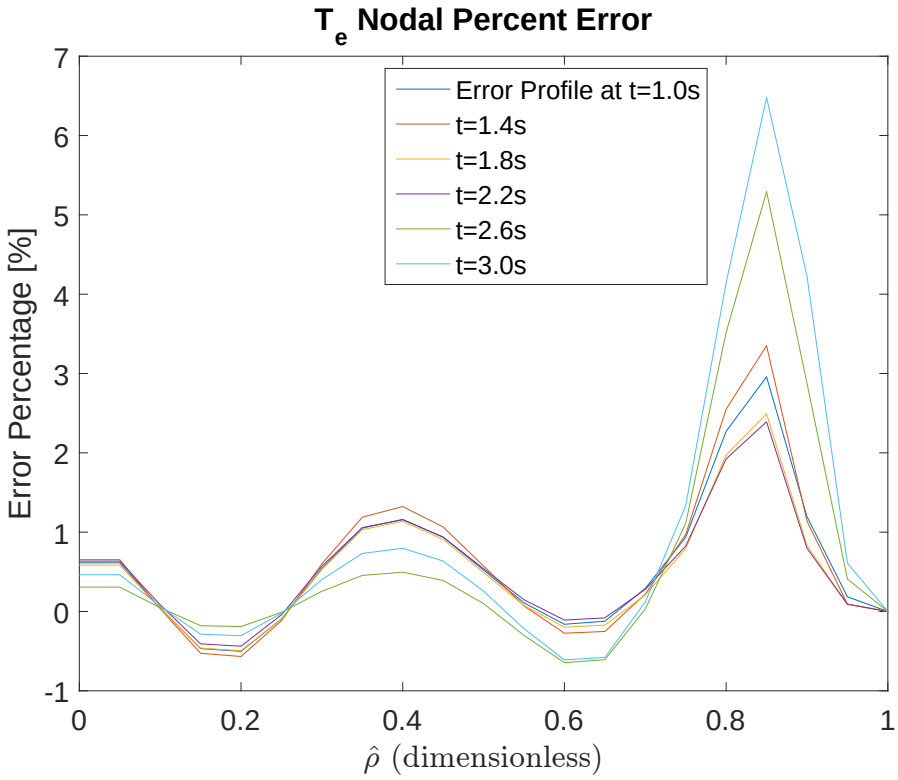

(a)

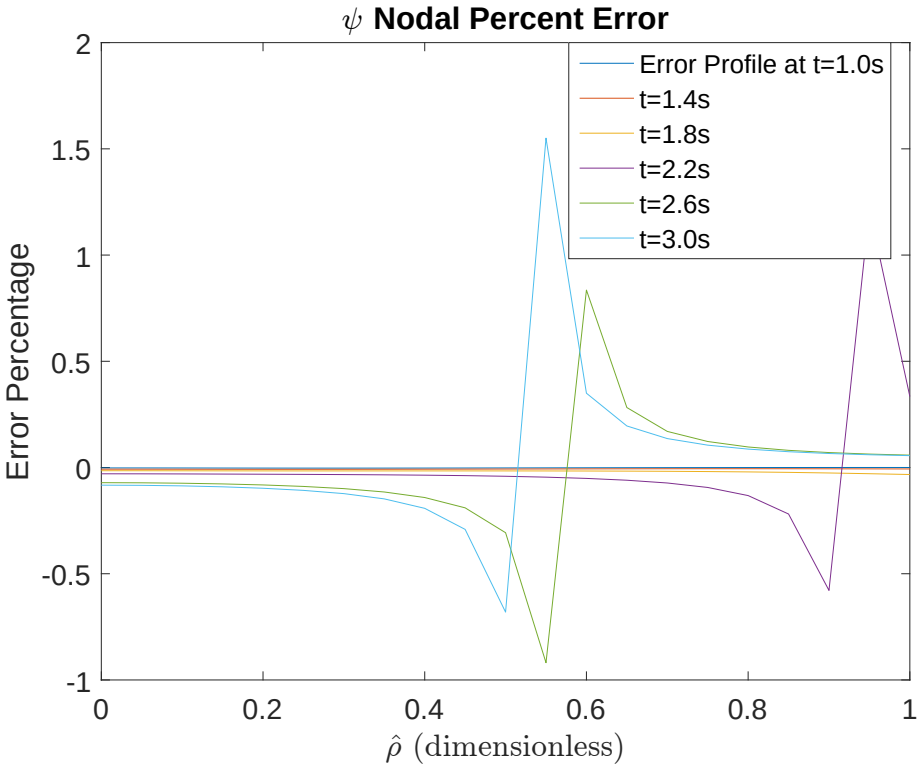

(b)

Figure 4.7: Error analysis for T_e (a) and ψ (b), when $\chi_e^{initial} = 0.6 * \chi_e^{target}$.

Test 3 (Flat Line as Initial Condition): Recalling from Chapter 3 the flat line initial condition test, $\chi_e^{initial}$ is given a constant value of 5 in this test. The resulting output is shown in Figure 4.8, where χ_e^{opt} and χ_e^{target} are compared, and the average error percentages have been calculated as

$$\begin{aligned} \delta_{ave}^{\chi_e} &= 7.70\% \\ \delta_{ave}^{T_e} &= 0.323\% \\ \delta_{ave}^{\psi} &= 2.41\% \end{aligned} \tag{4.4}$$

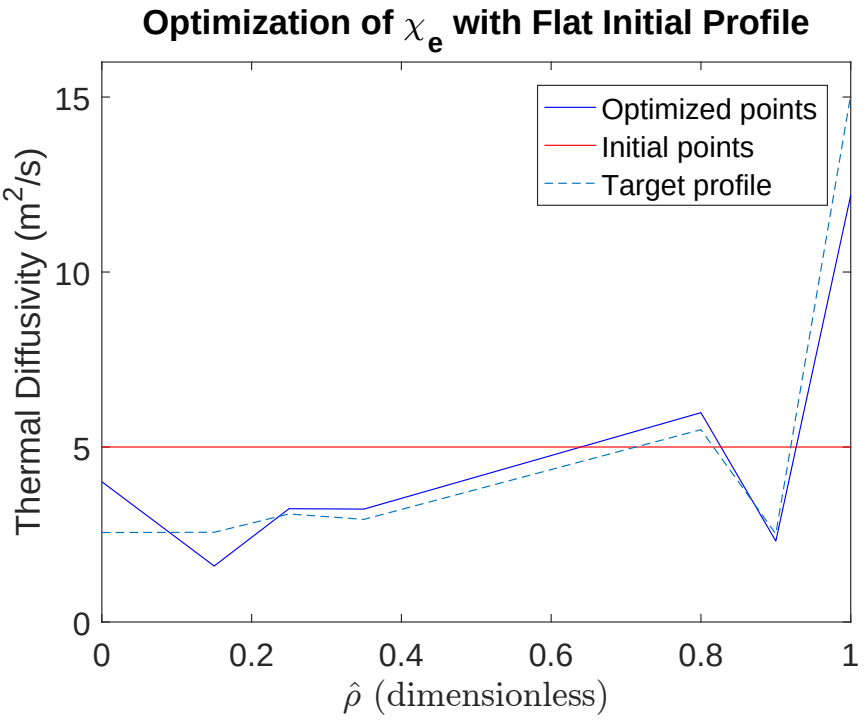

Figure 4.8: Comparison of χ_e^{opt} and χ_e^{target} profiles, modeled with $\chi_e^{initial}$ as 60% of the χ_e^{target} profile.

The resulting χ_e^{opt} is then used to predict both T_e^{opt} and ψ^{opt}, which are shown in Figure 4.9.

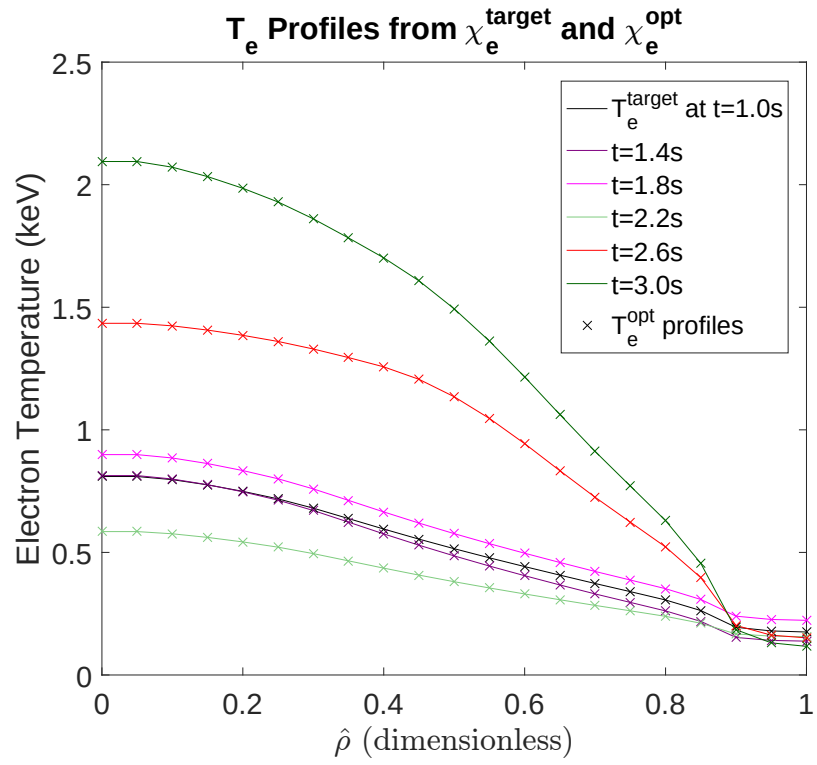

(a)

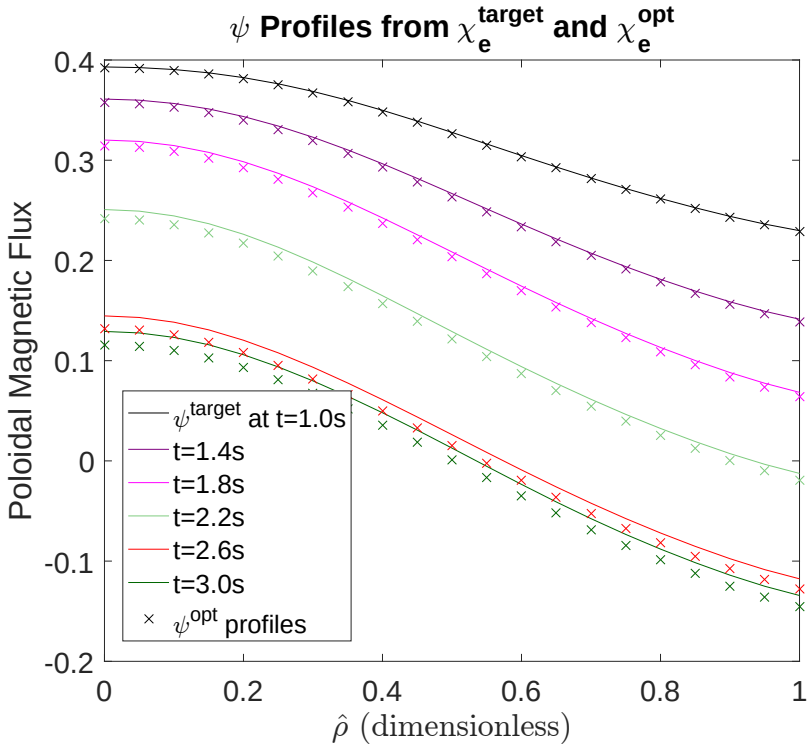

(b)

Figure 4.9: Compared target and simulated (a) temperature profiles and (b) magnetic flux profiles, with $\chi_e^{initial}$ as a flat line profile.

As in previous tests, we can show the error changing along the spatial domain in Figure 4.10, which exhibits a pattern similar to those in previous tests.

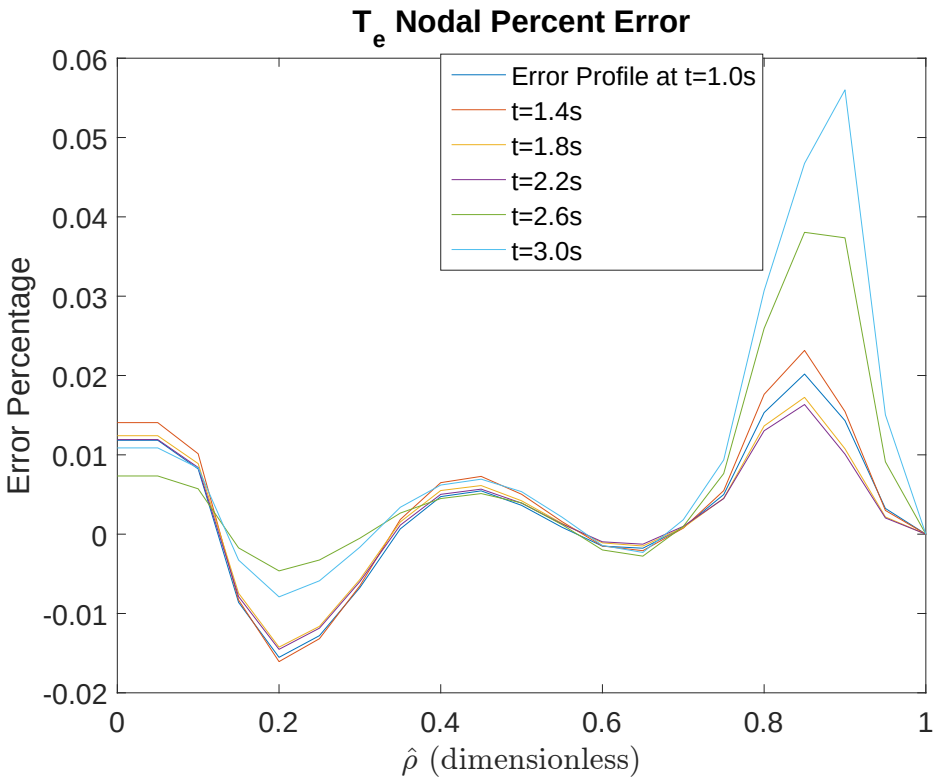

(a)

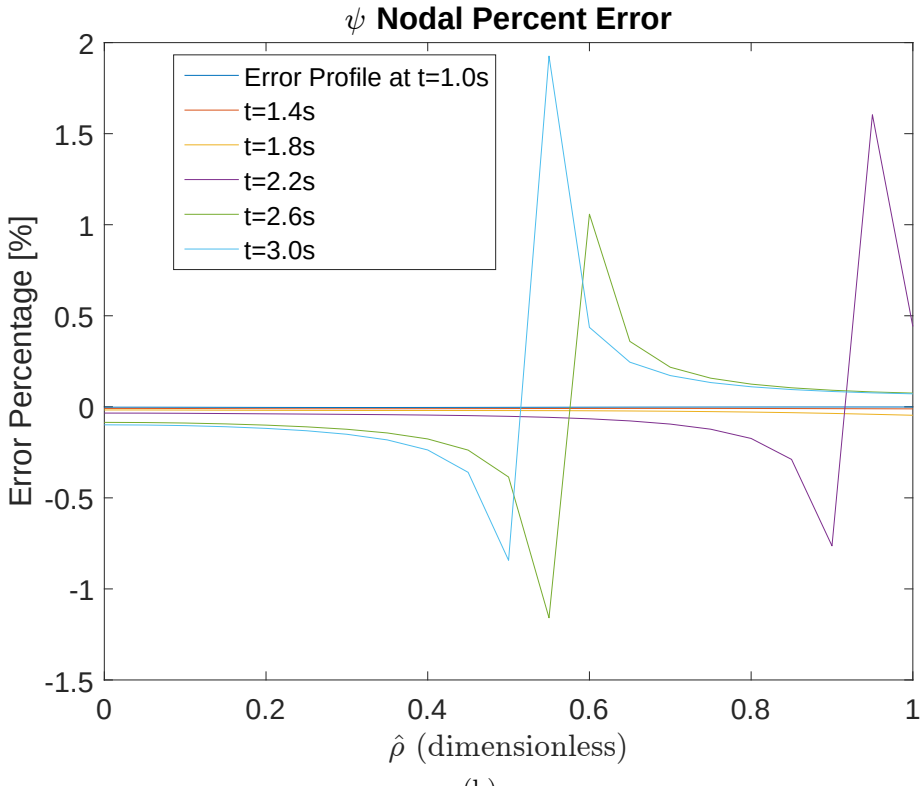

(b)

Figure 4.10: Error analysis for T_e (a) and ψ (b), when $\chi_e^{initial}$ = flat line.

4.3 Conclusions

In this chapter, a Sequential Quadratic Programming (SQP) optimization algorithm was once again implemented to estimate the thermal diffusivity profile. The to-be-optimized thermal diffusivity profile was parameterized exactly in the same way as in the previous chapter, i.e. it was modeled as a time-independent spatial profile reconstructed from values at seven spatial locations via interpolation. As a difference from the previous chapter, the to-be-minimized cost function was defined as the spatial-temporal integral of not only the quadratic error between predicted and target electron temperature profiles but also the quadratic error between predicted and target magnetic flux profiles. To carry out the optimization a numerical solver previously developed for the Magnetic Diffusion Equation (MDE), which governs the dynamics of the magnetic flux, was combined with the developed EHTE numerical solver. The to-be-matched electron temperature and magnetic flux profiles (target profiles) were constructed by numerically solving the EHTE and MDE using once again a time-averaged thermal diffusivity profile and simplified models for the geometric factors, electron density and heating sources.

The optimization algorithm was effective in converging to a thermal diffusivity profile that predicted temperature and flux profile evolutions closely matching the target profiles. Comparing the error profiles for all three tests, it appears that the initial thermal diffusivity profile has little effect on the ability of the SQP optimization algorithm to converge to a χ_e^{opt} that minimizes matching errors for both the electron temperature and the magnetic flux profiles. The $\delta_{ave}^{T_e}$ error is always below 1% and the δ_{ave}^{ψ} error fluctuates between 2-2.5%. This proves that the optimization algorithm, coupled with EHTE and MDE models, accurately identifies a χ_e^{opt}. However there is some room for improvement. Since the majority of error between predicted and target temperature profiles, as well as between predicted and target magnetic flux profiles, occurs in the range $0.5 \leq \hat{\rho} \leq 1$, additional critical points within this range could be added, and the deviation after $\hat{\rho} = 0.5$ could be more heavily weighted in the cost function.

Chapter 5

Optimizing χ_e Through Plasma State Scaling

5.1 Modeling and Estimation of χ_e

In the previous chapters, the to-be-optimized thermal diffusivity profile was parameterized by its value at several points in space. More precisely, the thermal diffusivity profile was modeled as a time-independent spatial profile and was reconstructed from values at seven spatial locations via interpolation. In this chapter, the thermal diffusivity profile is modeled as a time-dependent spatial function of critical properties of the plasma state. In this case, the thermal diffusivity profile is written as

$$\chi_e = (T_e)^{\alpha}(n_e)^{\beta}(q)^{\gamma} \tag{5.1}$$

where T_e represents the electron temperature, n_e denotes the electron density, and q represents the safety factor. The scaling factors α, β, and γ are the free parameters to be optimized by the algorithm in order to minimize the cost function, which is still defined as in (4.1). It is thus the goal of the SQP optimizer to converge on values for α, β, and γ that produce electron temperature and magnetic flux profiles matching their respective targets, which are generated as explained in Chapter 4.

5.2 Optimization Results

As with Chapters 3 and 4, we would like to find a χ_e^{opt} profile that minimizes the error between target and predicted temperatures and magnetic fluxes. However, in this case the thermal diffusivity is parameterized as in (5.1) in terms of 3 scaling factors instead of in terms of values at 7 spatial nodes. To determine initial guesses for the scaling factors α, β, and γ, it is important to examine the order of magnitude of each one of these factors, which are given by

$$\begin{aligned} T_e &\sim 10^0[keV] * 1.602 * 10^{-16}[J/keV] \\ n_e &\sim 10^{19}[m^{-3}] \\ q &\sim 10^0[dimensionless] \end{aligned} \tag{5.2}$$

Since the EHTE solver predicts electron temperatures in keV, the temperature units in (5.2) must be converted to Joules to achieve the $[W/s^2]$ units for χ_e. According to (5.1) and (5.2), in order to arrive at a diffusivity profile that ranges from 0 to 15, the electron density will have to be largely scaled down. Thus the initial values for the scaling constants are chosen as

$$[\alpha, \beta, \gamma] = [0.5, 0.005, 0.5] \tag{5.3}$$

With the initial guess in (5.3), the optimization algorithm converged to the following values for the scaling factors (for reference, computational processing time for this simulation was approximately 30 minutes):

$$[\alpha, \beta, \gamma] = [-0.0369, 0.0302, 0.2427] \tag{5.4}$$

Note that the sign for α was reversed, shifting the electron temperature factor to a fractional value. Figures 5.1-5.4 exhibit the results of this optimization.

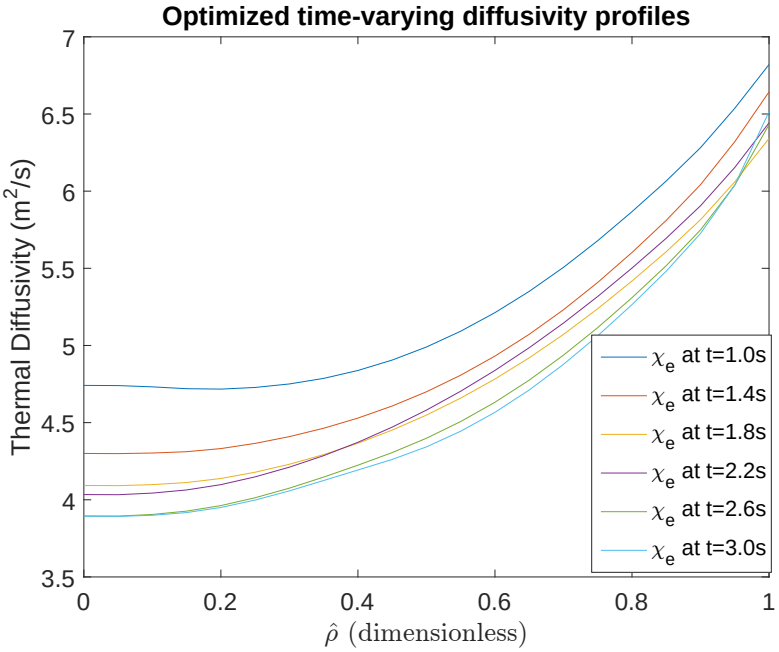

Figure 5.1: Optimized thermal diffusivity profiles at certain times.

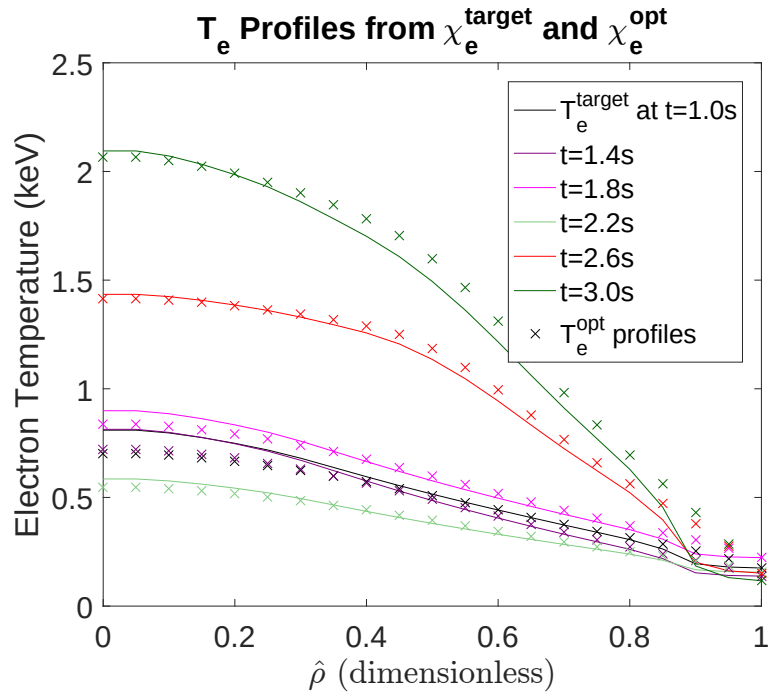

(a)

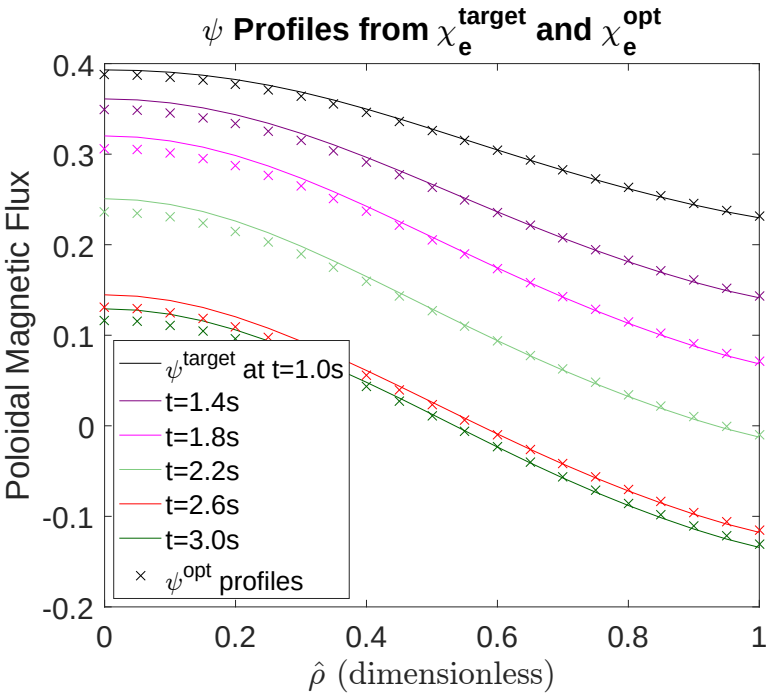

(b)

Figure 5.2: Comparison between target and optimized profiles for (a) electron temperatures and (b) magnetic flux, with χ_e^{opt} as the novel, equation-based profile.

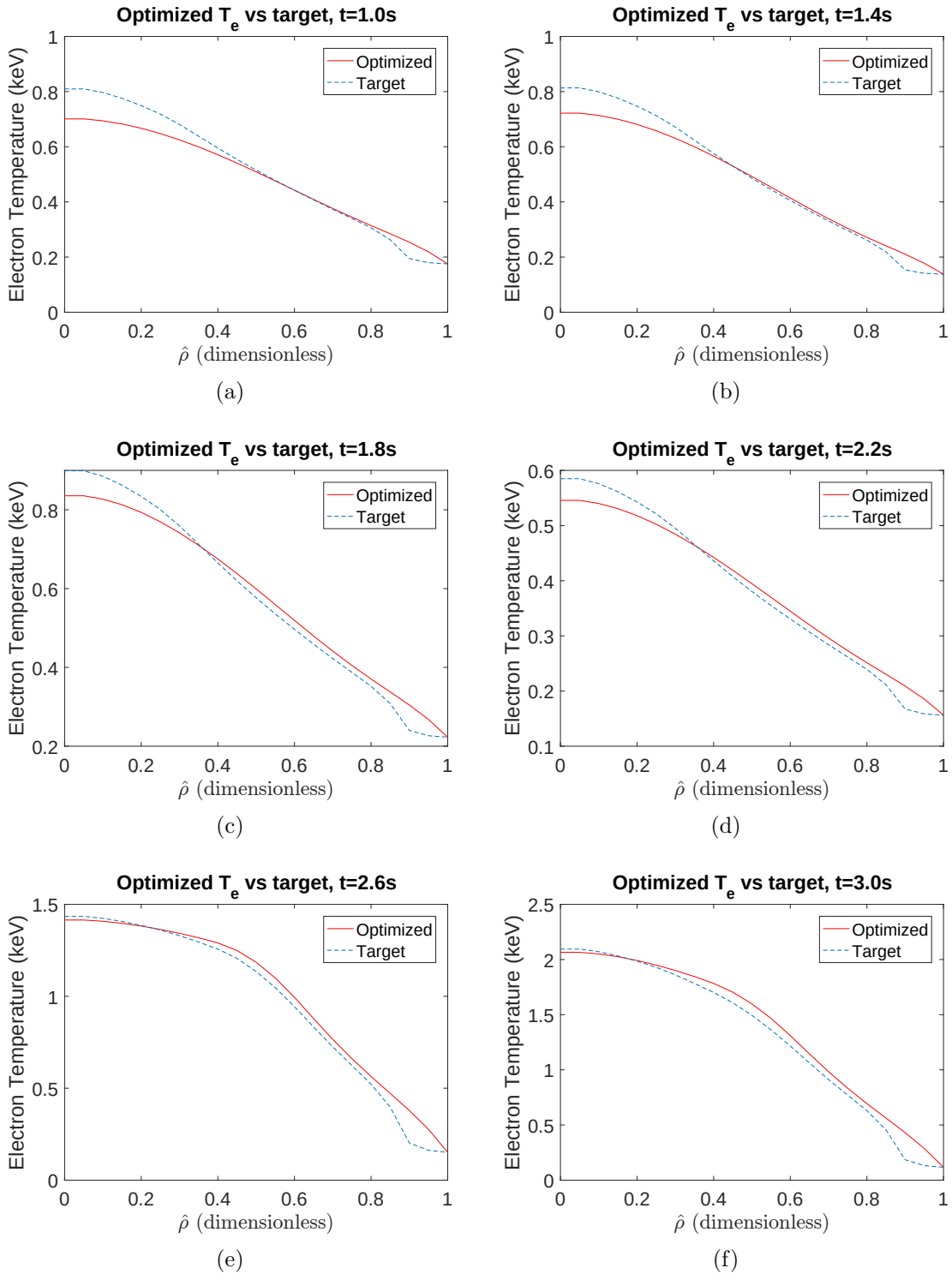

Figure 5.3: Comparison between optimized and target temperature profiles at (a) t=1.0s, (b) t=1.4s, (c) t=1.8s, (d) t=2.2s, (e) t=2.6s, (f) t=3.0s.

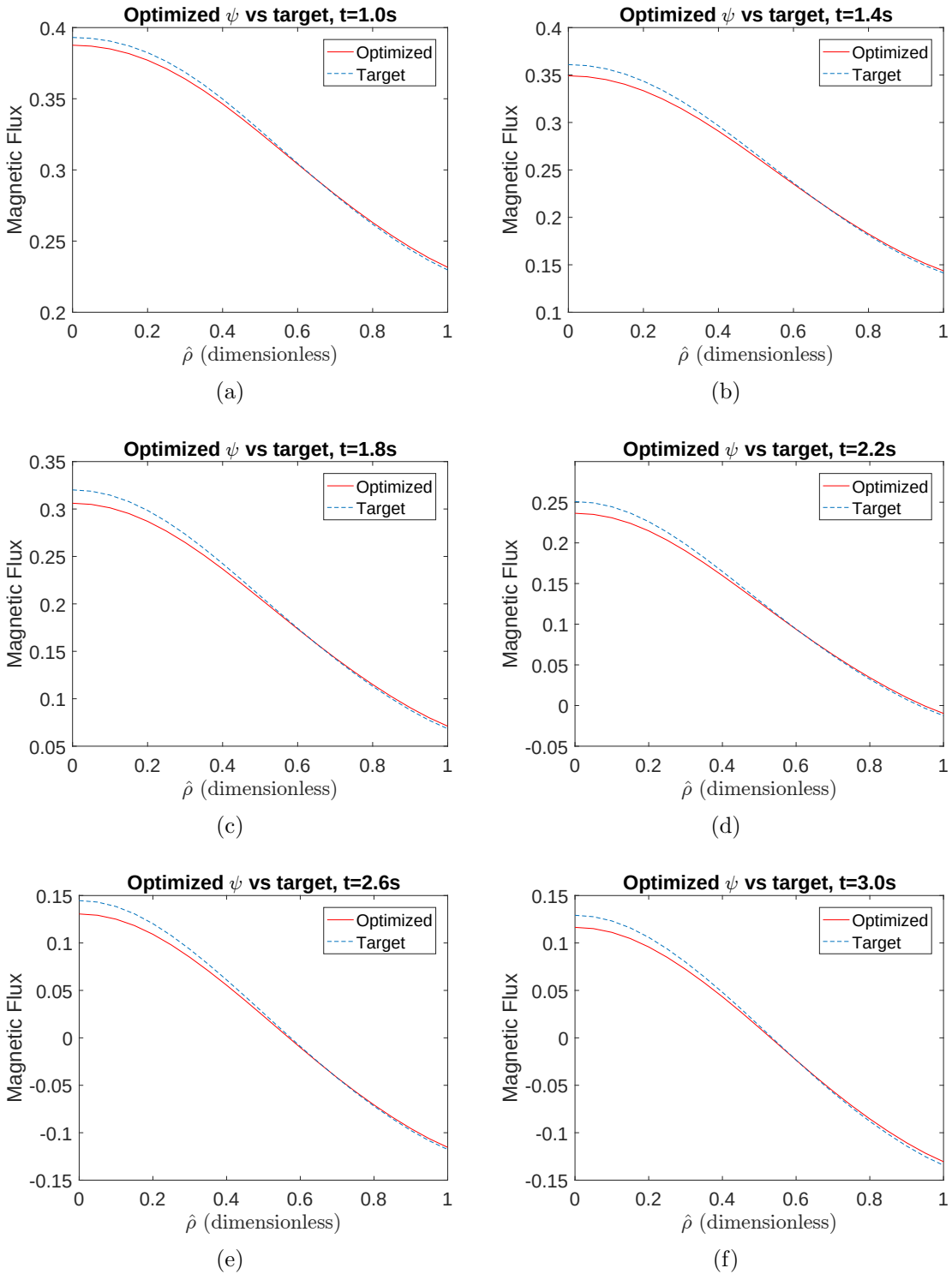

Figure 5.4: Comparison between optimized and target magnetic flux profiles at (a) t=1.0s, (b) t=1.4s, (c) t=1.8s, (d) t=2.2s, (e) t=2.6s, (f) t=3.0s.

A major difference between the results generated from the equation-based parameterization of χ_e in (5.1) and those in the previous chapters is that the thermal diffusivity is now modeled as a time-dependent profile instead of a time-constant profile. This better reflects actual conditions in a tokamak, where the plasma thermal diffusivity does change along the duration of the shot. From figures 5.2-5.4, it is clear that both the electron temperature and magnetic flux profiles try to match their target counterparts. However, the matching is probably not as good as in previous chapters with a different parameterization of χ_e. Figure 5.1 shows that the optimized χ_e profiles are radically different from the actual profiles (see Figure 2.8). Figure 5.5 displays the average χ_e^{opt} (Figure 5.1) compared against the average χ_e computed by TRANSP (Figure 2.8), which was denoted as χ_e^{target} in the previous chapters.

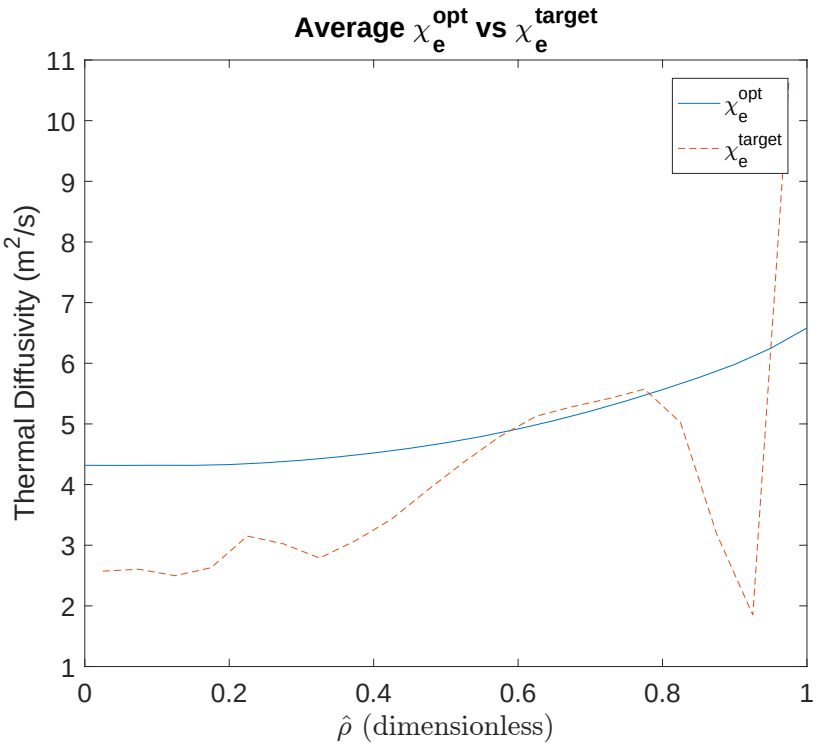

Figure 5.5: Average optimized thermal diffusivity profile from the new equation-based model compared against the average thermal diffusivity from TRANSP.

The difference shown in Figure 5.5 is clearly a consequence of the constraints imposed by the new parameterization. Where in the previous chapters the diffusivity dipped first and then spiked near the plasma boundary, in this case the diffusivity follows a smooth curve up to and through zone where a pedestal is expected. While it is important to point out the differences in the shapes of these two profiles, it should be noted that the goal of this work is not to match χ_e^{opt} with χ_e^{target}, but to come up with a simple model for χ_e as in (5.1) that predicts electron temperature and magnetic flux profiles in an approximate fashion. Thus, by analyzing the figures in 5.2 we can see that χ_e^{opt} satisfactorily approximates the T_e and ψ evolutions, but without capturing the pedestal near the plasma boundary (Figure 5.3).

Besides the specific constraints imposed by the parameterization itself, another reason for this discrepancy may reside on the equal spatial weighting assigned to the cost function. Let us examine the spatial dependence of the mismatch between optimized and target temperatures (one of the squared terms in the cost function). In (5.5), the difference between T_e^{opt} and T_e^{target} is calculated for a random time step (time index 60), i.e.

$$\begin{aligned} Error =& (T_e^{opt}(60,\hat{\rho}) - T_e^{target}(60,\hat{\rho}))^2 \\ =& [0.0040, 0.0040, 0.0034, 0.0025, 0.0016, 0.0010, 0.0003, \\ & 0.0000, 0.0001, 0.0003, 0.0005, 0.0006, 0.0005, 0.0004, \\ & 0.0004, 0.0003, 0.0003, 0.0009, 0.0042, 0.0017, 0.0000] \end{aligned} \tag{5.5}$$

which is graphically represented in Figure 5.6

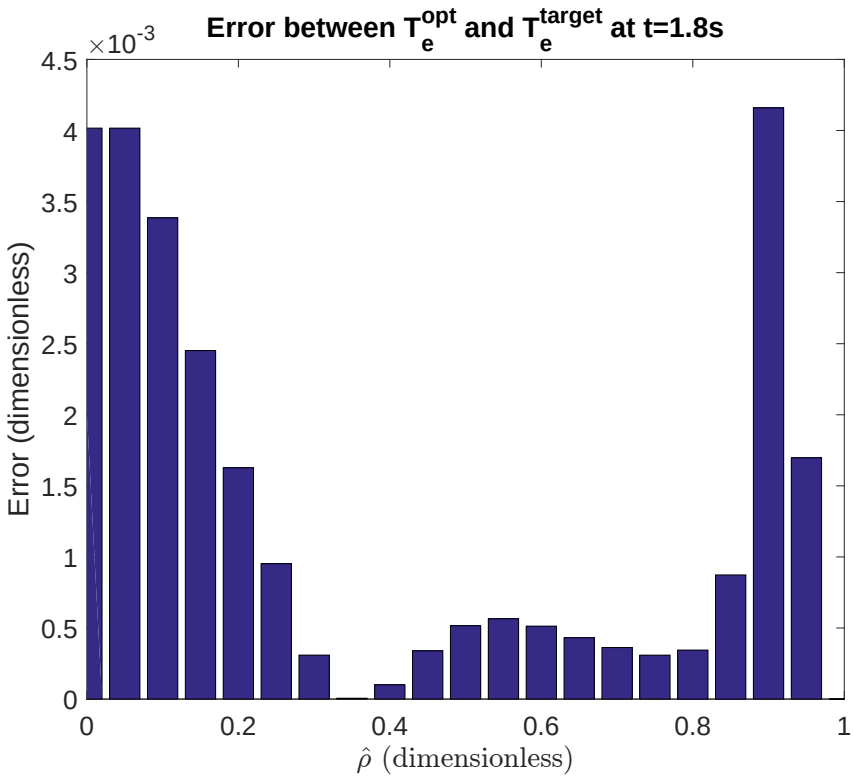

Figure 5.6: Squared difference between target and optimized electron temperatures at time t=1.8s.

From examining Figure 5.6, the majority of the error occurs in the inner region of the plasma (from the center of the plasma to halfway the distance towards the plasma boundary), with the exception of the spike occurring near the boundary. The optimization algorithm focuses on reducing this error, and the results is a neglected H-mode pedestal in the outer region of the plasma, as is clear in both the diffusivity and temperature/flux plots in Figures 5.1.-5.3. Refining the cost function by weighting more heavily the temperature mismatch at the spatial location where the pedestal is expected may help to capture this phenomenon. However, this corrective action may need to be accompanied by a different scaling for χ_e that could take into account its dependence on other plasma states.

5.3 Conclusions

In this chapter, a Sequential Quadratic Programming (SQP) optimization algorithm was once again implemented to estimate the thermal diffusivity profile. As a difference from previous chapters, the to-be-optimized thermal diffusivity profile was parameterized in a complete different way, i.e. it was modeled as a scaling law in terms of three critical properties of the plasma state, which results in a time-dependent spatial profile. The to-be-minimized cost function was defined as in Chapter 4, i.e. as the spatial-temporal integral of not only the quadratic error between predicted and target electron temperature profiles but also the quadratic error between predicted and target magnetic flux profiles. To carry out the optimization a numerical solver previously developed for the Magnetic Diffusion Equation (MDE), which governs the dynamics of the magnetic flux, was combined with the developed EHTE numerical solver. The to-be-matched electron temperature and magnetic flux profiles (target profiles) were constructed by numerically solving the EHTE and MDE using once again a time-averaged thermal diffusivity profile and simplified models for the geometric factors, electron density and heating sources.

The optimization algorithm was effective in converging to a thermal diffusivity profile that drives the temperature and flux profile evolutions close to their targets. However, a more pronounced mismatch in both electron temperature and magnetic flux profiles was observed in comparison with the results from previous chapters. This indicates the need to revise, and possibly augment, the plasma states entering the thermal diffusivity parameterization, which seems unable at the moment of capturing the strong variation in the thermal diffusivity that is needed to predict the temperature pedestal close to the plasma boundary. Nevertheless, the results are very promising because they show the feasibility to produce a very simple thermal diffusivity model that predicts electron-temperature and magnetic-flux evolutions with enough accuracy for control design.

Chapter 6

Conclusions and Future Work

6.1 Conclusions

The dynamics of the plasma electron temperature in a nuclear fusion reactor is governed by a partial differential equation called the Electron Heat Transport Equation (EHTE). Finite difference methods are frequently utilized to numerically solve nonlinear partial differential equations. The stability of the numerical solution depends on the type of finite difference technique implemented (implicit or explicit). In this work, a custom hybrid finite difference approach, which combines both implicit and explicit techniques, was developed to numerically solve the EHTE. The numerical solution was compared with predictions by TRANSP, a high-accuracy plasma transport code, to assess the ability of the developed numerical method to predict the electron temperature evolution in fusion plasmas.

Once a numerical method for the solution of the EHTE was developed and tested, a Sequential Quadratic Programming (SQP) optimization algorithm was implemented with the goal of identifying a thermal diffusivity profile, which is part of the EHTE, so that the evolutions of the electron temperature profile and the magnetic flux profile best match predefined profile evolutions. To carry out the optimization a numerical solver previously developed for the Magnetic Diffusion Equation (MDE), which governs the dynamics of the magnetic flux, was combined

with the developed EHTE numerical solver. The to-be-matched electron temperature and magnetic flux profiles, denoted as target profiles, were constructed by numerically solving the EHTE and MDE using the time-averaged thermal diffusivity profile over the duration of a specific discharge in DIII-D. The to-be-minimized cost function was defined as the spatial-temporal integral of the quadratic error between predicted (by the numerical solvers) and target electron temperature profiles. In some cases the quadratic error between predicted (by the numerical solvers) and target magnetic flux profiles was also included in the spatial-temporal integral. Given an initial guess for the thermal diffusivity profile, the optimization algorithm was capable of determining a profile minimizing the cost function.

The to-be-optimized thermal diffusivity profile was parameterized in two different ways. First, the thermal diffusivity profile was modeled as a time-independent spatial profile reconstructed from values at seven spatial locations via interpolation. The free parameters of the optimization algorithm were the seven values from which the whole thermal diffusivity profile was reconstructed. Second, the thermal diffusivity profile was modeled as a time-dependent spatial function of three critical properties of the plasma state, namely the electron temperature T_e, the electron density n_e, and the safety factor q. In this case, the thermal diffusivity profile was written as

$$\chi_e = (T_e)^{\alpha}(n_e)^{\beta}(q)^{\gamma}, \tag{6.1}$$

and the free parameters of the optimization algorithm were the scaling factors α, β, and γ. A plasma-state-dependent parameterization as the one proposed in (6.1) has the potential of producing a thermal diffusivity model valid for a larger range of plasma dischargers, i.e. for a larger range of plasma conditions.

6.2 Future Work

While the proposed optimization algorithm shows potential for modeling the thermal diffusivity in the EHTE, extensive additional work is needed to generalize the approach. First, since the model proposed in (6.1) has the capability of capturing the time evolution of the thermal diffusivity profile, the target profiles for the electron temperature and magnetic flux used in the to-be-minimized cost function should be generated using time-dependent thermal diffusivity profiles. These target profiles could be also obtained directly from more sophisticated plasma transport codes such as TRANSP. Second, the model parameterization obtained from one plasma discharge should be tested not only in that specific discharge but in other plasma discharges with similar magnetic geometries. These tests would determine the need for model refinement and optimization improvement. Third, in order to refine the proposed model, the need of incorporating additional properties of the plasma state in the parameterized model (6.1) should be assessed. Other plasma properties such as the magnetic shear can have an important impact on the evolution of the thermal diffusivity profile. As the number of plasma states incorporated in the parameterization of the thermal diffusivity increases, the number of scaling factors to be determined by the optimization algorithm also increases. Finally, in order to improve the optimization, data from more than just one discharge could be used to carry out the optimization. As more discharges are included in the optimization, the likelihood of determining a thermal diffusivity model with a large range of validity is increased.

Bibliography

[1] Barton J., Wehner W. *et al.*, "Simultaneous Closed-loop Control of the Current Porfile and the Electron Temperature Profile in the TCV Tokamak," *Proceedings of the 2015 American Control Conference,* Chicago, Illinois, USA, July 1-3, 2015

[2] Wehner W., Shi W., *et al.*, "First-Principle-Driven Model-Based Control of the Poloidal Magnetic Flux Profile at the DIII-D Tokamak," *19th IFAC World Congess*, Cape Town, South Africa, August 24-29, 2014

[3] Wesson, J., *Tokamaks*, Oxford, U.K.: Clarendon Press, 1997

[4] Wang H., Barton J. and Schuster E., "Current Density Profile Reconstruction in DIII-D Using Extended Kalman Filter," Unpublished

[5] Nocedal J. and Wright S.J., "Numerical Optimization", *Springer Series in Operations Research*, Springer-Verlag New York, 1999

[6] Pozrikidis C., "Numerical Computation in Science and Engineering", Oxford University Press, 1998, p. 526-579.

[7] Courant R., Friedrichs K., and Lewy H., "On the Partial Difference Equations of Mathematical Physics," *IBM J.* 11, 1967, p. 215-234

[8] Weisstein, Eric W., "Courant-Friedrichs-Lewy Condition", Math-World, [Online], Available:`http://mathworld.wolfram.com/Courant-Friedrichs-LewyCondition.html`

[9] Onjun T., Bateman G. and Kritz A.H., "Models for the pedestal temperature at the edge of H-mode tokamak plasmas," *Physics of Plasmas*, v 9, n 12, December 2002, p. 5018-5029.

[10] ITER, "External Heating Systems", [Online], Available: `https://www.iter.org/mach/Heating`

[11] Vietsciences, "Fusion Research", [Online], Available: `http://vietsciences.free.fr/giaokhoa/nangluong/nguyentuluc/fusion.htm`

[12] EuroFusion, "Heating the plasma: Research for tomorrow's energy supply", [Online], Available: `https://www.euro-fusion.org/fusion/spot-on-jet-operations/maintaining-the-plasma/heating-the-plasma/`

[13] Xu C., Ou Y. and Schuster E., "Transport Parameter Estimations of Plasma Transport Dynamics Using the Extended Kalman Filter," *IEEE Transactions of Plasma Science*, v 38, n 3, March 2010

[14] Boggs P. and Tolle Jon, "Sequential Quadratic Programming," *Acta Numerica*, 1996, p. 1-000.

[15] Mathworks, "Constrained Nonlinear Optimization Algorithms", [Online], Available: `http://www.mathworks.com/help/optim/ug/constrained-nonlinear-optimization-algorithms.html\#bqbgso0`

[16] Barton J., Shi W. *et al.*, "Physics-based Control-oriented Modeling of the Safety Factor Profile Dynamics in High Performance Tokamak Plasmas," *Proceedings of the 52nd IEEE Conference on Decision and Control,* Florence, Italy, December 10-13, 2013

[17] Barton J., Besseghir Karim., *et al.*, "Towards Semi-physical Model-based Control of the Magnetic and Kinetic Plasma Profile Evolution in the ITER Tokamak," Lehigh University and Association EURATOM-Suisse, Unpublished

Vita

Zachary Pelli, son of Joseph and Gail Pelli, was born in Stamford, Connecticut on December 7, 1992. He attended and recevied his Bachelor of Science in Mechanical Engineering from Lehigh University in May 2014. He also received a Minor in Aerospace Engineering from Lehigh University in May 2014. Zack is a member of the National Society of Collegiate Scholars, the National Association of Distinguished Professionals, and the Kappa Alpha Society. During the 2015-2016 period he worked at Lehigh University toward his MSc. degree under Prof. E. Schuster in the Plasma Control Laboratory. After completing his Master's degree he continued serving as CEO and owner of a startup mechanical engineering consulting company called PSO Consulting and located near Philadelphia, PA.